

XIT: Exploration and Exploitation Informed Trees for Active Gas Distribution Mapping in Unknown Environments

Mal Fazliu, Matthew Coombes, Sen Wang, and Cunjia Liu

Abstract—Mobile robotic gas distribution mapping (GDM) provides critical situational awareness during emergency responses to hazardous gas releases. However, most systems still rely on teleoperation, limiting scalability and response speed. Autonomous active GDM is challenging in unknown and cluttered environments, because the robot must simultaneously explore traversable space, map the environment, and infer the gas distribution belief from sparse chemical measurements. We address this by formulating active GDM as a next-best-trajectory informative path planning (IPP) problem and propose XIT (Exploration-Exploitation Informed Trees), a sampling-based planner that balances exploration and exploitation by generating concurrent trajectories toward exploration-rich goals while collecting informative gas measurements en route. XIT draws batches of samples from an Upper Confidence Bound (UCB) information field derived from the current gas posterior and expands trees using a cost that trades off travel effort against gas concentration and uncertainty. To enable plume-aware exploration, we introduce the gas frontier concept, defined as unobserved regions adjacent to high gas concentrations, and propose the Wavefront Gas Frontier Detection (WGFD) algorithm for their identification. High-fidelity simulations and real-world experiments demonstrate the benefits of XIT in terms of GDM quality and efficiency. Although developed for active GDM, XIT is readily applicable to other robotic information-gathering tasks in unknown environments that face the exploration and exploitation trade-off.

Index Terms—Gas distribution mapping, active sensing, informative path planning, next-best-trajectory, frontier exploration.

I. INTRODUCTION

In the event of a gas leak, timely and reliable acquisition of gas dispersion information is critical to assessing risk and responding effectively; any delay can have serious consequences for human safety and environmental integrity [1]. At the scene, gas concentration levels are regarded as the most valuable raw data that can be measured. To gather this information, mobile robotic platforms equipped with chemical and perceptual sensors are a standard choice, as they can access polluted and uncertain areas unsafe for humans and withstand harsher conditions. Still, these platforms offer limited value without a tool to localise each concentration reading and reconstruct a gas distribution model. Gas source localisation (GSL) methods, such as source term estimation, face challenges in unknown environments where structural mapping is required, and are further limited in indoor or cluttered settings without

M. Fazliu, M. Coombes, and C. Liu are with the Department of Aeronautical and Automotive Engineering, Loughborough University, Leicestershire, UK, LE11 3TU (e-mails: {m.fazliu2, m.coombes, c.liu5}@lboro.ac.uk).

S. Wang is with the Department of Electrical and Electronic Engineering, Faculty of Engineering, Imperial College London, South Kensington Campus, London, UK, SW7 2AZ (e-mail: sen.wang@imperial.ac.uk).

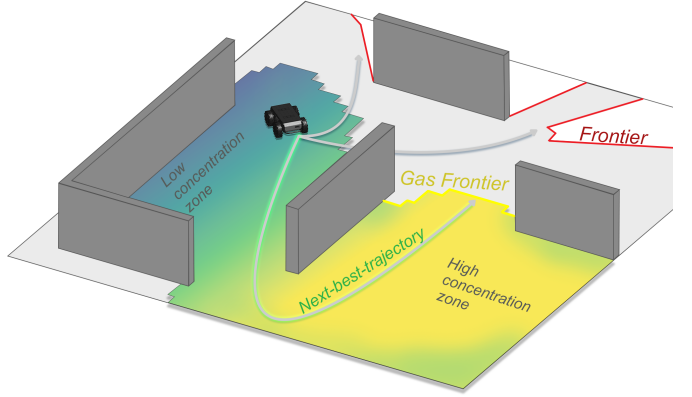


Fig. 1. Overview of the XIT planner for active GDM. The figure illustrates a robot constructing a gas distribution map from concentration measurements in real time and planning gas-exploitive, distance-aware trajectories toward both gas frontiers and environmental frontiers. The three candidate paths generated by XIT are shown in grey, with the next-best trajectory (NBT) highlighted in green, representing the path with the highest expected information value, balancing gas dispersion inference and spatial exploration where possible.

a prevailing wind field or when dealing with complex multi-source releases [2]. In such scenarios, gas distribution mapping (GDM) provides an alternative by constructing spatial maps of gas concentration from spatiotemporal chemical measurements [3].

Many GDM algorithms have been developed for robotic gas sensing and mapping [3–7]. One popular representation is the Gaussian Markov random field (GMRF) model [3], as it is able to efficiently encode gas measurements and spatial dispersion within a factor graph framework, which naturally accommodates obstacle effects, making it suitable for cluttered or indoor environments. Recently, [8] solved this factor graph online using Gaussian belief propagation (GBP) [9], demonstrating scalable real-time GDM in both two and three dimensions in unknown environments through performing structural mapping on a teleoperated mobile robot.

While remote operation demonstrates the potential of online robotic GDM in realistic scenarios, the next key step is removing this reliance on teleoperation. Remote operation requires specialists on hand, which can slow response times in critical situations. There is therefore strong incentive to pursue an autonomous GDM solution that offers faster response and improved performance through informative path planning (IPP) [10, 11], that is, an active sensing principle that closes the loop by actively selecting sensing locations as the gas distribution belief and structural mapping evolve. We refer to this closed-loop paradigm as *active GDM*.

Previous studies on IPP for GDM focus on gas inference and address exploiting gas-rich regions and gas map coverage, but often fall short in real-world settings due to two main limitations: (i) the computational or modelling limitations of the GDM function and (ii) the assumption of a known map of the environment. As discussed, the former has lately been mitigated through scalable inference using GBP for the GMRF [8]. The latter, however, remains largely unaddressed even within the broader field of active information gathering or mapping, under which active GDM falls. In this domain, sampling-based planners [12] are typically employed to optimise an information-theoretic objective, such as entropy or mutual information, to determine the next-best trajectory (NBT) or the next-best view (NBV) for the robot to execute. Yet, they generally focus on their primary information gathering objectives, either targeting exogenous fields (e.g., pollution, radiation) assuming a known obstacle map [13, 14], or focussing on structural exploration to build 3D geometry or semantic representations [15–18]. For active GDM, a realistic planner must simultaneously uncover the unknown environment while deciding where to effectively collect informative gas measurements.

To address this gap, we propose an active GDM framework for unknown and cluttered environments, where the robot must reason about multi-modality sensor information and balance exploration and exploitation objectives. These objectives include: (i) environmental exploration, encouraging the robot to explore its surroundings to build a geometric map and uncover areas that may contain gas; (ii) gas structure exploration, probing newly discovered gas regions to explore the extent and shape of the plume; and (iii) gas exploitation, revisiting high value gas regions to improve confidence in the GDM model. An illustration depicting the mobile robot performing active GDM with the solution presented in this paper is included in Fig. 1. Our strategy is structured around guiding the robot toward exploration-rich destinations while simultaneously exploiting valuable information en route. Inspired by the decoupling principle for active simultaneous localisation and mapping (SLAM) in [19], the proposed framework first generates a set of informative paths to each exploratory goal, then selects the NBT to execute.

At the core of this framework, we introduce Exploration and Exploitation Informed Trees (XIT), a multi-objective, sampling-based planner adapted from batch informed trees (BIT*) [20] that facilitates our NBT approach for active GDM in unknown environments. XIT constructs quasi-simultaneous paths toward goal regions selected for their exploration potential, while exploiting key gas regions en route through information-guided sampling and tree expansion, such that each generated trajectory jointly addresses exploration and exploitation objectives. Sampling is performed over an upper confidence bound (UCB) map derived from the current gas state estimate, and tree expansion is guided by a UCB-distance cost function that favours regions of high gas concentration, high uncertainty, and low travel cost. By integrating informed sampling with guided tree expansion, XIT limits expansion into less informative areas, thereby reducing unnecessary search effort and yielding high-quality paths to each goal.

Contributions. The main contributions of this work are:

- **XIT**, a sampling-based IPP planner for active GDM that balances exploration and exploitation by generating informed paths toward exploration-rich goal regions using a gas-informed objective for both sampling and tree expansion, tailored to gas exploitation;
- To our knowledge, the first **active GDM system** that jointly reasons about environmental exploration, gas structure exploration, and gas exploitation, validated through high-fidelity simulation and a real world gas leak experiment;
- **gas frontier**, a novel concept for detecting plume boundaries to support plume-aware exploration, and the Wavefront Gas Frontier Detection (WGFD) algorithm for their identification.

II. RELATED WORK

Path planning approaches for GDM have historically utilised predetermined coverage trajectories, such as lawnmower sweeps, that do not adapt based on observed gas distributions [5, 21–23]. These fixed patterns fail to efficiently leverage the impact of measurement locations on GDM accuracy. IPP addresses this by adaptively selecting sensing positions that evolve with the current gas distribution belief.

Early IPP approaches for GDM iteratively selected individual sampling locations based on the current gas distribution estimate. The first explicit use of IPP for GDM appears in [24], where an adaptive sensing strategy based on artificial potential fields balanced exploitation of high-concentration and high-variance regions with gas map coverage via repulsive forces from previous measurements, converging faster than fixed sweeps. They utilised the Kernel DM [25] for GDM, a lightweight data-driven method that was popular at the time, in particular the DM+V/W variant [26] which incorporates wind information but not temporal dependencies. The main drawback of Kernel DM (and its variants) has been its inconvenience in accounting for obstacle effects on the plume. In [27], several reward functions were examined using the original GMRF formulation [3], which permits effective obstacle modelling, facilitating IPP for GDM in cluttered environments to be tested and validated using a gas release CFD dataset. A* search was employed to compute distance-based traversal costs between the sampling goal locations. The most effective reward combined concentration with time-weighted joint uncertainty, yielding substantially faster convergence than a non-adaptive sweep. Ercolani et al. [28] focused on 3D GDM and opted for the Kernel DM+V/W algorithm, citing its lightweight computational demands and the lack of a scalable solver for GMRF at the time. They evaluated IPP methods that prioritised uncertainty and variability rather than exploiting high-concentration regions, including Lévy flight, entropy-based, and Kullback-Leibler divergence (KLD) criteria. While these strategies produced detailed maps over limited areas, they exhibited suboptimal exploratory behaviour, becoming trapped in locally informative regions and failing to achieve broader coverage. To address this limitation, they introduced a clustering algorithm using K-means to partition the operational

space into k clusters visited sequentially, enforcing broader coverage while maintaining adaptive sampling within each cluster.

More recent work has addressed planning with non-myopic forward simulation [29] and multi-waypoint trajectory execution [30]. A GSL technique known as infotaxis was adapted to GDM in [29] using partially observable Markov decision process (POMDP) planning with the gas and wind (GW) variant of the GMRF [31], which was computed using a sparse direct solver. The approach performs finite-horizon forward simulation to evaluate multi-step action sequences in the four cardinal directions (N, W, S, E) using a KLD-based reward, executing the first action before replanning in a receding horizon manner. Forward simulation requires evaluating GW-GMRF multiple times per planning cycle, which the authors acknowledge restricts real-time applicability. A two-phase low-to-high resolution framework using GMRF with GBP was proposed in [30], first performing sparse sampling to identify high-concentration regions, then selecting the highest-reward cells and planning distance-optimised trajectories through them for dense sampling within fixed time budgets. While this framework executes complete multi-waypoint paths, it rigidly separates exploration and exploitation into sequential phases rather than considering both objectives within each trajectory.

Of the aforementioned works, [24], [28], and [30] do not consider obstacles in their planning, while [27] and [29] assume prior knowledge of the environment via predetermined occupancy maps. These assumptions limit applicability to realistic emergency response scenarios, where unknown and cluttered environments necessitate joint reasoning about environmental exploration in conjunction with effective gas distribution inference. Even GSL, the alternative approach to gas distribution modelling that has been more extensively studied [2], struggles to address the full problem. Recent work, such as [32, 33], has extended IPP to GSL in unknown environments, yet such methods are typically formulated assuming a fixed number of sources, most often a single source. This limits generalisability when source configurations are unknown, even in state-of-the-art approaches that leverage GDM to update beliefs over source parameters in known environments [7]. The only work to address unknown environments for GDM is [34], which performs online occupancy grid mapping (OGM) alongside Kernel DM+V [5] for GDM. Their system uses a finite state machine that switches between frontier exploration and gas exploitation based on manually tuned thresholds. In gas mode, a single high-cost cell is selected and an RRT-based planner generates a collision-free path to it. While the planner accounts for obstacles, the underlying Kernel DM+V model does not, and unlike [30], only the goal location is informed by the current gas belief, not the trajectory.

In this work, we propose XIT, a sampling-based planner that generates candidate informed trajectories considering both environmental exploration and gas inference objectives, and selects the most informative among them. This aligns with the next-best-trajectory concept [16], introduced for autonomous exploration in unknown environments, where RRT-based expansion generates multiple frontier-reaching paths and trajectories are selected by trading off information gain

against distance and actuation cost. XIT generalises this idea into a more unified and ordered approach for active GDM, drawing inspiration from BIT* [20] but operating from a next-best-vertex expansion perspective during tree expansion. Unlike standard BIT*, which expands toward a single goal, XIT supports concurrent expansion toward multiple occupancy and gas frontiers. Moreover, unlike [16], tree growth in XIT is informed, with gas exploitation incorporated directly into expansion through a UCB-based cost function. Crucially, by operating within a GDM formulation, XIT avoids assumptions about the number or location of gas sources, making it applicable to a wide range of complex and multi-source scenarios.

III. ACTIVE GDM: FORMULATION AND SYSTEM

This section formalises the representations and planning concepts used throughout our active GDM framework. We first describe how the environment and gas fields are modelled, then introduce the frontier-based goal regions that drive exploration, and finally outline the next-best-trajectory formulation and the overall system architecture (see Fig. 2) that support online decision making.

A. Environment and Gas Representation

We consider the problem in a planar configuration space with unknown, static obstacles. Let the robot's configuration space be $\mathcal{X} \subset \mathbb{R}^2$, with $\mathcal{X}_{\text{obs}} \subset \mathcal{X}$ denoting obstacle regions and $\mathcal{X}_{\text{free}} := \mathcal{X} \setminus \mathcal{X}_{\text{obs}}$ denoting the true free space. Let $\mathbf{x}_k \in \mathcal{X}_{\text{free}}$ represent the robot's state at planning time step $k \in \mathbb{N}$. To represent the environment structure, we maintain an occupancy grid map $\mathcal{M}_k^{\text{occ}}$ on a lattice \mathcal{C} , where each cell $c \in \mathcal{C}$ has an occupancy belief $p_k(c)$. Each state $\mathbf{x} \in \mathcal{X}$ corresponds to a unique cell $c(\mathbf{x}) \in \mathcal{C}$, which allows us to write map quantities directly as functions of \mathbf{x} , e.g., $p_k(\mathbf{x}) := p_k(c(\mathbf{x}))$. The known-free subset at step k is the union of cells whose occupancy probability is below a free threshold τ_{free} , i.e.,

$$\hat{\mathcal{X}}_{\text{free}}(k) := \bigcup_{c: p_k(c) \leq \tau_{\text{free}}} c \subset \mathcal{X}_{\text{free}}. \quad (1)$$

In this work, planning is restricted to $\hat{\mathcal{X}}_{\text{free}}(k)$; unknown cells are not traversed. The robot pose is assumed to be available, for example from a SLAM solution. Given such a pose estimate, an occupancy grid map can be constructed using LiDAR or RGB-D sensors through a standard inverse sensor model with ray tracing.

Analogous to the occupancy map, the gas distribution $\mathcal{M}_k^{\text{gas}}$ is represented by a GMRF posterior (μ_k, Σ_k) defined on the same lattice (or a coarser one). This posterior can be obtained by processing gas sensor data collected up to step k using, e.g., direct solvers [3] or belief propagation [8]. The GMRF representation further supports per-state statistics, with mean $\mu_k(\mathbf{x})$ and variance $\varepsilon_k(\mathbf{x})$ available on $\hat{\mathcal{X}}_{\text{free}}(k)$, as cells marked occupied or unknown in $\mathcal{M}_k^{\text{occ}}$ impose structural constraints in the graph.

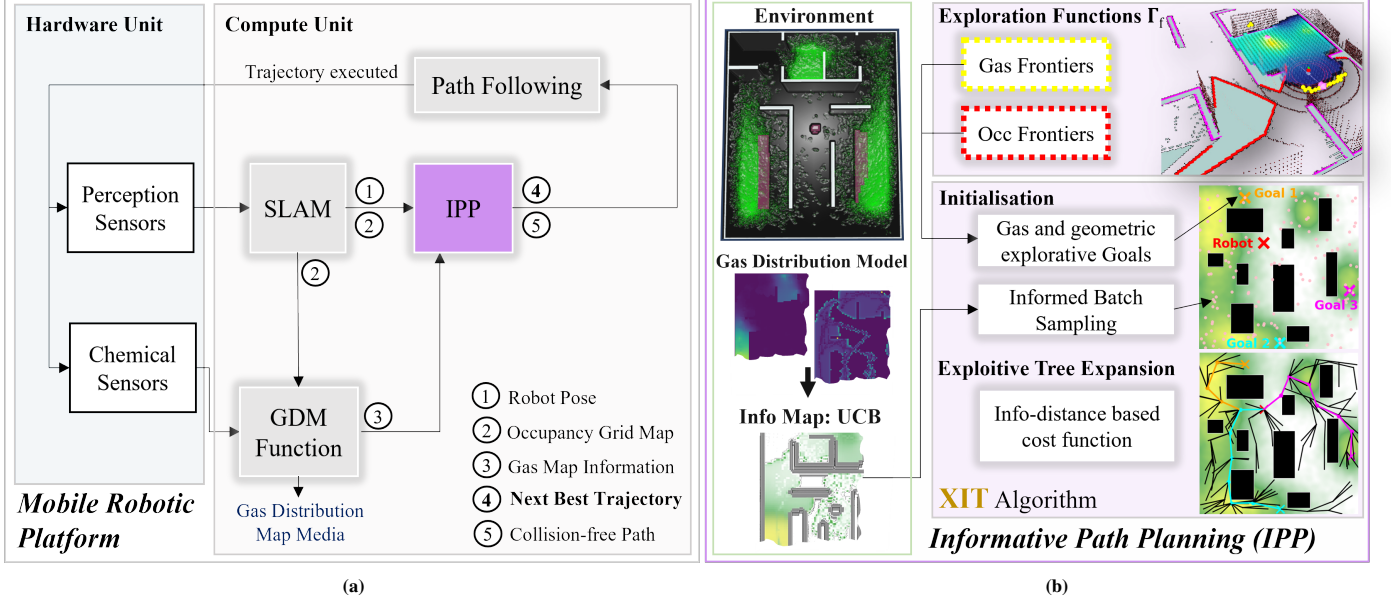


Fig. 2. System overview of the proposed active GDM framework. On the left (a) is a general system architecture for the mobile robotic application. Key functional components in the compute unit include localisation and mapping for navigation and occupancy information (summarised as the SLAM module), the GDM function, and the IPP module, which selects the NBT. The IPP process is expanded in (b), where we also illustrate a gas polluted environment and the corresponding mean and uncertainty maps produced during GDM. The concept of gas frontiers is visualised using yellow markers along the boundary of the estimated gas plume, while conventional frontiers outlining the unknown occupancy map are in red. Both types are used by XIT to steer and terminate tree expansion in exploration rich regions, while a UCB-based cost function, derived from the current gas model, guides paths through inferred high value gas areas. A separate example is included to illustrate the characteristic trajectories and tree structure generated by XIT.

B. Frontier-based Goal Regions

To enable exploration of both the unknown physical environment and the gas structure, we adopt frontier detection techniques [35] to identify goal regions for the robot to move toward. The occupancy frontiers $\mathcal{F}_k^{\text{occ}}$ denote the set of frontier clusters, where each frontier $f^{\text{occ}} \in \mathcal{F}_k^{\text{occ}}$ is a contiguous group of cells on the boundary between known and unknown space in the occupancy map. These regions drive the expansion of the robot's reachable free space. Inspired by the role of frontiers in guiding environment exploration, we introduce *gas frontiers*, denoted $\mathcal{F}_k^{\text{gas}}$, defined analogously as a set of gas-frontier clusters $f^{\text{gas}} \in \mathcal{F}_k^{\text{gas}}$, each representing the boundary of a high-concentration gas region adjacent to unobserved gas states. A detailed description of the gas-frontier detection procedure is provided in Section V.

The exploration-rich goal set is then

$$\mathcal{G}_k = \mathcal{F}_k^{\text{occ}} \cup \mathcal{F}_k^{\text{gas}}. \quad (2)$$

That is, the collection of all occupancy and gas frontier clusters.

C. Next-best Trajectory Planning

To formalise the planning problem, we model an admissible trajectory as an absolutely continuous curve

$$\sigma : [0, 1] \rightarrow \hat{\mathcal{X}}_{\text{free}}(k),$$

starting at the robot's current state, $\sigma(0) = \mathbf{x}_k$, and terminating in one of the frontier-based goal regions, $\sigma(1) \in \mathcal{G}_k$. Our goal is to choose a trajectory σ from \mathbf{x}_k that enables the

robot to efficiently collect observations along the path, improving both the occupancy grid map and the gas distribution model; in particular, expanding known-free space (environment exploration), expanding the critical gas region (gas structure exploration), and reducing gas uncertainty around high-concentration regions (gas exploitation).

Executing a trajectory produces new measurements, and these updates are captured by an online mapping operator

$$\Phi : (\mathcal{M}_k(\cdot); \sigma) \mapsto \mathcal{M}_{k+1}(\cdot), \quad (3)$$

which performs the occupancy-grid update and the GMRF inference based on the data gathered along σ .

Solving the full non-myopic IPP problem, which can be cast as a POMDP [29], is intractable due to the coupled evolution of the occupancy and gas models. Finite-horizon approximations are also difficult to justify in this setting. Non-myopic evaluation first requires forecasting future occupancy states with geometric map prediction techniques like in [36]. Propagating the GMRF through these anticipated obstacles compounds uncertainty and in turn reduces the reliability of information-gain estimates, while adding significant computational overhead. As a first solution to the active GDM problem, our premise is that the robot obtains more reliable information by acting on its current beliefs and re-planning in real time after executing the selected trajectory, rather than relying on non-myopic predictions over uncertain futures. We therefore adopt a myopic, information-aware NBT formulation. At each planning iteration k , the robot selects the next best trajectory

$$\sigma_k^* = \arg \min_{\sigma \in \Sigma_k} J_k(\sigma), \quad \text{s.t. } \sigma(0) = \mathbf{x}_k, \sigma(1) \in \mathcal{G}_k. \quad (4)$$

Here, the set Σ_k contains only collision-free trajectories, and $J_k(\sigma)$ is a strictly positive, monotonically increasing, additive cost function that promotes gas exploitation by favouring trajectories through informative regions. Exploration of new space and critical gas structure is induced through the frontier-based goal set \mathcal{G}_k . After executing σ_k^* in full, the models are updated via the mapping operator Φ in Eq. (3), yielding \mathcal{M}_{k+1} , and the optimisation in Eq. (4) is then resolved at iteration $k+1$.

This recursive NBT formulation captures the autonomy principle of our system: trajectories are guided through information-rich regions while maintaining progress toward frontier-based goals. The result is the first unified approach to the inherent exploration-exploitation problem which arises when closing the loop in GDM. The key components of the optimisation in Eq. (4), namely the candidate set Σ_k , the cost function $J_k(\sigma)$, and the frontier-derived goal set \mathcal{G}_k , must be designed cooperatively to ensure effective environmental exploration and gas inference within active GDM.

D. System Architecture and Components

Before presenting the algorithms in detail, we provide a high-level overview of the proposed active GDM system. As shown in Fig. 2, the framework combines gas sensing, OGM, online GDM, IPP via XIT, and a path-following module to execute the selected trajectory.

At the core of this architecture is the IPP formulation in Eq. (4), which determines the next best trajectory based on frontier-derived goal regions and a cost function that promotes gas exploitation while remaining sensitive to travel cost. The associated sample-based solver, XIT, constructs a single information-guided tree whose branches grow toward all selected goal regions in parallel fashion, expanding only through known-free space and avoiding obstacles.

Unlike GSL approaches that face challenges in unknown environments, particularly indoors or under multi-source releases [2], XIT is well suited to active gas inference in unknown environments without requiring assumptions about source number or location. Its tree exploits informative gas regions en route, while frontier-based goal selection promotes gas-structure or environmental exploration at the destination.

IV. EXPLORATION-EXPLOITATION INFORMED TREES

XIT is a sampling-based search planner inspired by the principles of BIT* [20], but adapted for information-driven planning toward multiple exploration-rich goals. We refrain from using the term multi-goal, which in the literature typically refers to finding a single path that visits all goals, as our formulation instead constructs independent trajectories in the set Σ_k to each goal in \mathcal{G}_k in parallel. Like BIT*, XIT incrementally builds an explicit search tree within an implicit random geometric graph (RGG), but here the vertices are drawn from a biased sampling distribution over the free space, guided by an underlying information map. The search is ordered by a cost function combining path cost with heuristic estimates to each goal, ensuring that the most promising states are expanded first.

Unlike BIT*, which alternates between dense sampling batches and search phases to iteratively refine a single solution, XIT grows the tree in a single continuous expansion process until admissible paths to each goal region are found or the search queue is exhausted. Given our problem setting, operating in unknown environments with partially constructed and therefore expanding maps, we argue that repeatedly refining paths to already discovered goals offers little benefit, for reasons analogous to our choice of a myopic approximation in the problem formulation. As the robot executes the selected NBT, the occupancy and information maps evolve, so refinements beyond feasibility often yield diminishing or irrelevant gains. The focus is therefore on generating information-guided trajectories toward all exploration-rich destinations as early as possible.

A. XIT: Problem Formulation

The notation used in the formulation and presentation of XIT (Alg. 1) is defined in this subsection, along with algorithm inputs and assumptions. The notation introduced in Section III is carried over where applicable. We fix a planning step k and adopt the active GDM formulation in Eq. (4). For notational simplicity, we drop the index k on all quantities except \mathbf{x}_k , which denotes the current robot state.

Let $\mathcal{T} := (V, E)$ denote the explicit search tree, where $V \subset \mathbf{X}_s \cup \{\mathbf{x}_k\} \cup \mathcal{G}$ is the set of vertices and $E = \{(\mathbf{v}, \mathbf{w})\}$ is the set of edges connecting vertices $\mathbf{v}, \mathbf{w} \in V$. The associated vertex and edge queues are denoted by Q_v and Q_e , respectively, and store candidate vertices and edges to be processed during the search.

The quantity $g_\tau(\mathbf{x})$ denotes the cost-to-come within the current search tree, with states not in the tree assigned a cost of ∞ . If $g(\mathbf{x})$ is the optimal cost-to-come to $\mathbf{x} \in \hat{\mathcal{X}}_{\text{free}}$, then by definition $g_\tau(\mathbf{x}) \geq g(\mathbf{x})$, $\forall \mathbf{x} \in \hat{\mathcal{X}}_{\text{free}}$. The heuristic $\hat{h}(\mathbf{x})$ is an admissible estimate of the cost from \mathbf{x}_k to a state \mathbf{x} for which $\exists \mathbf{X}_{\text{goal}}^{(j)} \subset \mathcal{G}$ s.t. $\mathbf{x} \in \mathbf{X}_{\text{goal}}^{(j)}$. The search ordering function, responsible for determining the next vertex to expand, is defined as

$$\hat{f}(\mathbf{x}) := g_\tau(\mathbf{x}) + \hat{h}(\mathbf{x}). \quad (5)$$

For an edge (\mathbf{x}, \mathbf{y}) , $c(\mathbf{x}, \mathbf{y})$ is the true cost and $\hat{c}(\mathbf{x}, \mathbf{y})$ is an admissible estimate, where

$$\hat{c}(\mathbf{x}, \mathbf{y}) \leq c(\mathbf{x}, \mathbf{y}) \leq \infty, \quad (6)$$

with edges intersecting obstacles or unknown cells in the occupancy map \mathcal{M}^{occ} assigned infinite cost.

The sampling set \mathbf{X}_s is a finite subset of the known free space,

$$\mathbf{X}_s \subset \hat{\mathcal{X}}_{\text{free}},$$

obtained from an informed sampling procedure based on an information distribution \mathcal{I} . In the active GDM setting, \mathcal{I} is derived as a scalar information field $\mathcal{I}(\mathbf{x})$ from the gas map \mathcal{M}^{gas} on $\hat{\mathcal{X}}_{\text{free}}$, with its specific form introduced later in Section IV-C.

The exploration module Γ_f encapsulates the frontier construction introduced in Section III-B. In this work, Γ_f returns

both occupancy frontiers and gas frontiers. Occupancy frontiers are obtained using standard frontier-based exploration techniques such as fast frontier detection (FFD) [35], whereas gas frontiers are extracted using the WGFD procedure developed later in Section V. For planning, each such region is represented by a nominal goal state $\mathbf{x}_{\text{goal}}^{(j)}$ and a corresponding goal set $\mathbf{X}_{\text{goal}}^{(j)} \subset \mathbf{X}_s$, for example the k_n nearest samples in \mathbf{X}_s to $\mathbf{x}_{\text{goal}}^{(j)}$. We collect the nominal goal states in the set

$$\mathbf{x}_{\text{goals}} = \{\mathbf{x}_{\text{goal}}^{(1)}, \mathbf{x}_{\text{goal}}^{(2)}, \dots\},$$

and the associated sample-based goal sets are written

$$\mathcal{G} = \{\mathbf{X}_{\text{goal}}^{(1)}, \mathbf{X}_{\text{goal}}^{(2)}, \dots\}.$$

We do not distinguish notationally between a frontier cluster and its sample-based representation when this causes no ambiguity. XIT itself is agnostic to how these goal regions are prioritised; it simply operates on the set provided by the exploration module. In practice, when only a limited number of goal regions are used for planning, different goal-selection policies may be applied, such as prioritising gas frontiers over occupancy frontiers or vice versa. A collection of these policies is evaluated in our high-fidelity experiments in Section VI.

The Lebesgue measure of a set is denoted $\lambda(\cdot)$, and ξ_n denotes the Lebesgue measure of the unit n -dimensional ball. The notation $|\cdot|$ represents the cardinality of a set. We write $\mathbf{X} \leftarrow^+ \{\mathbf{x}\}$ and $\mathbf{X} \leftarrow^- \{\mathbf{x}\}$ to concisely denote the set operations $\mathbf{X} \leftarrow \mathbf{X} \cup \{\mathbf{x}\}$ (insertion) and $\mathbf{X} \leftarrow \mathbf{X} \setminus \{\mathbf{x}\}$ (removal), respectively.

B. Algorithm

The algorithm is divided into an initialisation phase and a multi-direction expansion phase.

1) *Initialisation* (Alg 1, Lines 1:7): Alg. 1 begins by generating N informed samples from the information distribution $\mathcal{I} : \hat{\mathcal{X}}_{\text{free}} \rightarrow \mathbb{R}_{\geq 0}$, producing the set \mathbf{X}_s . The exploration module Γ_f is then invoked to return the nominal goal states $\mathbf{x}_{\text{goals}}$. For each \mathbf{x}_{goal} , we form a sample-based goal set $\mathbf{X}_{\text{goal}} \subset \mathbf{X}_s$ by selecting the k_n nearest samples in \mathbf{X}_s . Next, the root node \mathbf{x}_k initialises the tree's vertex set V and vertex queue Q_v , while the edge set E and edge queue Q_e both begin empty. The connection radius r_N for edge search (Alg. 1, Line 7) can be chosen in line with [12, 20], with γ larger than a RGG threshold, such that

$$\gamma_{\text{RGG}} = 2 \left(1 + \frac{1}{n} \right)^{\frac{1}{n}} \left(\frac{\lambda(\hat{\mathcal{X}}_{\text{free}})}{\xi_n} \right)^{\frac{1}{n}} \quad (7)$$

2) *Multi-direction Tree Expansion Procedure* (Alg 1, Lines 8:28): Tree expansion occurs until either Q_v is empty or a feasible path from the root to every goal set $\mathbf{X}_{\text{goal}} \in \mathcal{G}$ has been found. As delineated from line 9 of Alg. 1, the algorithm cycles through the goal sets, expanding vertices incrementally for each \mathbf{X}_{goal} rather than completing one region before moving to the next. If a feasible path to a \mathbf{X}_{goal} has already been determined, i.e., there exists $\mathbf{x} \in \mathbf{X}_{\text{goal}}$

Algorithm 1: XIT ($N, \mathbf{x}_k, \Gamma_f, \mathcal{I}$)

```

1  $\mathbf{X}_s \leftarrow \text{InformedSample}(N, \mathcal{I})$  // Section IV-C;
2  $\mathbf{x}_{\text{goals}} \leftarrow \Gamma_f();$ 
3 for  $\mathbf{x}_{\text{goal}}$  in  $\mathbf{x}_{\text{goals}}$  do
4    $\mathbf{X}_{\text{goal}} \leftarrow \{\mathbf{x} \in \mathbf{X}_s \mid$ 
     $\mathbf{x}$  is among the  $k_n$  nearest to  $\mathbf{x}_{\text{goal}}\};$ 
5    $\mathcal{G} \leftarrow^+ \mathbf{X}_{\text{goal}};$ 
6  $V \leftarrow \mathbf{x}_k; E \leftarrow \emptyset; Q_e \leftarrow \emptyset; Q_v \leftarrow V;$ 
7  $r_N \leftarrow \gamma \left( \frac{\log(|\mathbf{X}_s|)}{|\mathbf{X}_s|} \right)^{\frac{1}{n}};$ 
8 while  $Q_v \neq \emptyset \& g_\tau(\mathbf{x}) \in \mathcal{G} = \infty$  do
9   for  $\mathbf{X}_{\text{goal}}$  in  $\mathcal{G}$  do
10    if  $Q_v \neq \emptyset \& g_\tau(\mathbf{x}) \in \mathbf{X}_{\text{goal}} < \infty$  then
11      continue
12    else
13       $\mathbf{v}_m \leftarrow \arg \min_{\mathbf{x} \in Q_v} g_\tau(\mathbf{x}) + \hat{h}(\mathbf{x});$ 
14       $Q_v \leftarrow^- \mathbf{v}_m;$ 
15       $V_{\text{near}} \leftarrow \{\mathbf{w} \in \mathbf{X}_s \mid \|\mathbf{v}_m - \mathbf{w}\|_2 \leq r_N\};$ 
16       $Q_e \leftarrow^+ \{(\mathbf{v}_m, \mathbf{w}) \in V_{\text{near}}\};$ 
17      while  $Q_e \neq \emptyset$  do
18         $\mathbf{w}_m \leftarrow \arg \min_{\mathbf{w} \in Q_e} \hat{c}(\mathbf{v}_m, \mathbf{w}) + \hat{h}(\mathbf{w});$ 
19         $Q_e \leftarrow^- (\mathbf{v}_m, \mathbf{w}_m);$ 
20        if  $g_\tau(\mathbf{v}_m) + \hat{c}(\mathbf{v}_m, \mathbf{w}_m) < g_\tau(\mathbf{w}_m)$  then
21          if  $g_\tau(\mathbf{v}_m) + c(\mathbf{v}_m, \mathbf{w}_m) < g_\tau(\mathbf{w}_m)$ 
22            then
23              if  $\mathbf{w}_m \in V$  then
24                 $E \leftarrow \{(\mathbf{v}, \mathbf{w}_m) \in E\};$ 
25              else
26                 $V \leftarrow^+ \mathbf{w}_m;$ 
27                 $Q_v \leftarrow^+ \mathbf{w}_m;$ 
28                 $E \leftarrow^+ (\mathbf{v}_m, \mathbf{w}_m);$ 
29      return  $(V, E);$ 

```

with $g_\tau(\mathbf{x}) < \infty$, the algorithm advances to the next goal region without any additional action in the present iteration. Otherwise, tree expansion continues towards any \mathbf{X}_{goal} yet to yield a solution (Alg. 1, Lines 13:27). Although the nominal stopping condition requires every $\mathbf{X}_{\text{goal}} \in \mathcal{G}$ to admit a finite-cost path from the root, the quasi-simultaneous cyclic processing of all goal sets also permits earlier termination. Even when some goal sets remain unreached, the tree will already have extended branches in their direction. In practice, this yields partial, goal-directed solutions at any time, with the final NBT solution quality improving as computation proceeds.

In the absence of a feasible path to an \mathbf{X}_{goal} , the expansion step begins by selecting the state $\mathbf{x} \in Q_v$ with the smallest value of the current tree cost-to-come plus heuristic cost-to-go, yielding the expansion node \mathbf{v}_m (Alg. 1, Line 13). Incorporating the tree cost-to-come into this ordering ensures that branch

growth is guided by the most promising information available. Once selected, the corresponding state \mathbf{v}_m is removed from Q_v . The neighbourhood V_{near} is then constructed by collecting all states $\mathbf{w} \in \mathbf{X}_s$ within radius r_N of \mathbf{v}_m , where r_N denotes the maximum admissible edge length. Candidate edges $(\mathbf{v}_m, \mathbf{w})$ are subsequently inserted into Q_e for processing.

XIT follows a next-best-vertex expansion scheme. Once the vertex \mathbf{v}_m is selected, all of its neighbouring edges are examined in a single full-expansion step. This design choice promotes multi-directional exploration, since expanding an entire neighbourhood often introduces vertices into Q_v that may become promising expansion vertices \mathbf{v}_m for subsequent \mathbf{X}_{goal} in later iterations. The outgoing edges \mathbf{w} in Q_e are processed in order of the minimal estimated cost-to-go from \mathbf{v}_m to the state in \mathbf{X}_{goal} that yields the lowest heuristic cost when reached via \mathbf{w} (Alg. 1, Line 18). This ordering facilitates early detection of a goal-reaching edge, allowing the search to terminate without processing the remaining, less promising edges. The selected edge is then removed from Q_e . Admission of the edge is governed by the criteria in Alg. 1, Lines 20–21, where compliance with these conditions dictates acceptance into the tree. If \mathbf{w}_m is not yet present in the tree, compliance in Alg. 1, Line 20 is guaranteed because $g_\tau(\mathbf{w}_m)$ evaluates to ∞ . Following this scenario, provided the edge is collision-free, \mathbf{w}_m is added to both V and Q_v , and the edge $(\mathbf{v}_m, \mathbf{w}_m)$ is inserted into E (Alg. 1, Lines 25:27). Should \mathbf{w}_m already exist in the tree, a potential rewiring step is triggered. Its previous parent edge $(\mathbf{v}, \mathbf{w}_m)$ is removed (Alg. 1, Line 23) and replaced by $(\mathbf{v}_m, \mathbf{w}_m)$ whenever the actual cost $c(\mathbf{v}_m, \mathbf{w}_m)$ yields a lower arrival cost. As per the notation defined in Section IV-A, any collision along the edge results in $c(\mathbf{v}_m, \mathbf{w}_m) = \infty$. To reduce unnecessary computation, this collision check is deliberately delayed until Alg. 1, Line 21. The estimated cost $\hat{c}(\mathbf{v}_m, \mathbf{w}_m)$ is first evaluated to ascertain whether progressing to the more expensive collision test is warranted.

C. Information Field and Cost Design for Gas Exploitation

This subsection details the design of the information field, informed sampling mechanism, cost formulation, and associated heuristics used to construct gas-exploitative paths, while the exploration module that provides the goal regions is presented separately in Section V.

Information field and informed sampling: Let $\mu(\mathbf{x})$ and $\varepsilon(\mathbf{x})$ denote the posterior gas mean and variance introduced in Section III-A. We define the UCB information field as

$$\mathcal{I}(\mathbf{x}) = \tilde{\mu}(\mathbf{x}) + \beta \varepsilon(\mathbf{x}), \quad (8)$$

where the parameter $\beta \geq 0$ balances exploiting high concentration and exploring regions of high variance in the gas map. The normalised mean concentration is defined as

$$\tilde{\mu}(\mathbf{x}) = \frac{\mu(\mathbf{x})}{\max_{\mathbf{z} \in \hat{\mathcal{X}}_{\text{free}}} \mu(\mathbf{z})}, \quad (9)$$

where the denominator is strictly positive. Similarly, we normalise \mathcal{I} over $\hat{\mathcal{X}}_{\text{free}}$ as

$$\begin{aligned} \hat{\mathcal{I}}(\mathbf{x}) &= \frac{\mathcal{I}(\mathbf{x}) - \mathcal{I}_{\min}}{\mathcal{I}_{\max} - \mathcal{I}_{\min}}, \\ \mathcal{I}_{\min} &= \min_{\mathbf{z} \in \hat{\mathcal{X}}_{\text{free}}} \mathcal{I}(\mathbf{z}), \quad \mathcal{I}_{\max} = \max_{\mathbf{z} \in \hat{\mathcal{X}}_{\text{free}}} \mathcal{I}(\mathbf{z}). \end{aligned} \quad (10)$$

where, as before, $\max_{\mathbf{z} \in \hat{\mathcal{X}}_{\text{free}}} \mu(\mathbf{z}) > 0$.

The InformedSample function draws exactly N unique states with probability proportional to $\hat{\mathcal{I}}$, assigning zero probability to occupied cells, unknown cells, and the robot's current cell. This forms the batch \mathbf{X}_s (Alg. 1, Line 1).

Why UCB rather than uncertainty alone: Using only $\varepsilon(\mathbf{x})$ would target unobserved areas regardless of concentration, which spreads effort and neglects critical regions. The UCB field \mathcal{I} couples mean and variance, so the planner revisits high concentration areas to reduce uncertainty where it matters, i.e. enables the exploitation of the critical gas regions.

Cost function and heuristics: Since the planner minimises a positive, additive cost, high-UCB regions must correspond to low cost. We therefore define the information penalty as the complement of the normalised information field

$$P(\mathbf{x}) = 1 - \hat{\mathcal{I}}(\mathbf{x}). \quad (11)$$

For any tree edge $(\mathbf{x}, \mathbf{y}) \in E$, the edge cost is

$$c(\mathbf{x}, \mathbf{y}) = \sum_{\mathbf{p} \in \mathcal{S}(\mathbf{x}, \mathbf{y})} P(\mathbf{p}) + \alpha \|\mathbf{y} - \mathbf{x}\|_2, \quad (12)$$

where $\mathcal{S}(\mathbf{x}, \mathbf{y})$ is a discrete set of points along the straight segment from \mathbf{x} to \mathbf{y} . The information can be evaluated at vertices only, provided the maximum edge length r_N is fixed, or accumulated along edges to capture information on the line, as in Eq. (12). The parameter $\alpha \geq 0$ weights travel distance relative to information. As per the notation defined, if any point in $\mathcal{S}(\mathbf{x}, \mathbf{y})$ lies in an obstacle or unknown cell, the cost is infinite. A sufficient choice for the heuristic $\hat{h}(\mathbf{x})$ is a distance-only lower bound to the goal region \mathbf{X}_{goal} , which we adopt in the analysis of Section IV-D. In practise, to provide UCB-aware search guidance, $\hat{h}(\mathbf{x})$ can instead use the same UCB penalty-distance structure toward the goal region \mathbf{X}_{goal} , selecting \mathbf{y} as the goal state $\mathbf{x} \in \mathbf{X}_{\text{goal}}$ that provides the best cost taken. Note that an exploration cost associated with \mathbf{X}_{goal} , for example a frontier utility, could be incorporated into the heuristic. We omit this here for simplicity to avoid cluttering the new components, though it is a natural extension.

Next-best trajectory cost: Given Σ , the batch of collision free candidate trajectories from XIT, the NBT problem in Eq. (4) is completed by the following trajectory cost.

For a discrete trajectory $\sigma = [\mathbf{x}_0, \dots, \mathbf{x}_H]$, define the edge set $\Psi(\sigma) := \{(\mathbf{x}_i, \mathbf{x}_{i+1})\}_{i=0}^{H-1}$. The trajectory cost is

$$J(\sigma) = \sum_{(\mathbf{x}', \mathbf{y}') \in \Psi(\sigma)} \left[\sum_{\mathbf{p} \in \mathcal{S}(\mathbf{x}, \mathbf{y})} P(\mathbf{p}) + \alpha \|\mathbf{y}' - \mathbf{x}'\|_2 \right]. \quad (13)$$

Here primes indicate the two vertices of each edge in $\Psi(\sigma)$, and \mathbf{p} ranges over the discrete set of points along the segment joining \mathbf{x}' and \mathbf{y}' . If one wished to evaluate information only

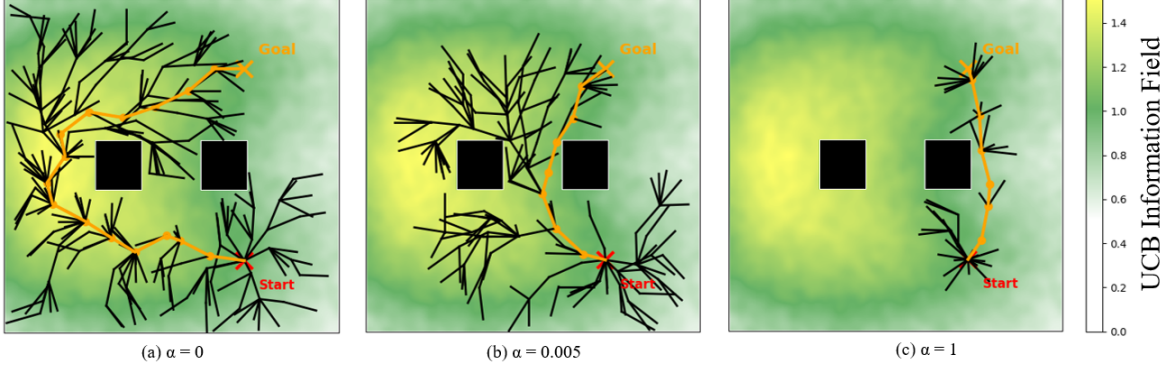


Fig. 3. Effect of the distance weight α on an isolated XIT trajectory. The three panels use the same scenario, informed sample size (N), start, and goal, with $\alpha = 0$ (a), $\alpha = 0.005$ (b), and $\alpha = 1$ (c). Larger α yields a shorter path that de-emphasises high-information corridors, trading exploitation for reduced travel.

at the vertices, the inner summation over $\mathcal{S}(\mathbf{x}, \mathbf{y})$ would be removed and P taken at the vertices instead.

As an example, we include Fig. 3 to illustrate the role of the distance weight parameter α on an isolated trajectory.

D. Algorithm Properties

This subsection discusses the theoretical properties of the proposed XIT algorithm, particularly on the probabilistic completeness (PC) and (almost-sure) asymptotic optimality (AO). The analysis follows the random-geometric-graph (RGG) machinery commonly used in the sampling-based planning [12], and the view of ‘‘search over an implicit RGG’’ from BIT* [20].

To facilitate the analysis, we assume the samples \mathbf{X}_s are drawn i.i.d. from a mixture distribution

$$q(\mathbf{x}) = (1 - \varepsilon) \hat{\mathcal{I}} + \varepsilon \frac{1}{\lambda(\hat{\mathbf{X}}_f)}, \quad (14)$$

where $\hat{\mathcal{I}}$ is the UCB-based importance density normalised on $\hat{\mathbf{X}}_f$ and $\varepsilon \in (0, 1)$ is a small positive constant. The second term is a uniform distribution to ensure $q(\mathbf{x})$ has non-zero density everywhere in $\hat{\mathbf{X}}_f$. In practice, the informed distribution $\mathcal{I}(\mathbf{x})$ based on UCB can be used by adding a small positive variance followed by normalisation on $\hat{\mathbf{X}}_f$.

Theorem 1 (Probabilistic completeness of XIT): Assume $\hat{\mathbf{X}}_f \subset \mathbb{R}^n$ is open and bounded, and choose one goal region $\mathbf{X}_{\text{goal}}^{(j)} \subset \hat{\mathbf{X}}_f$ of non-zero measure. Suppose there exists a δ -clear collision-free curve from the current state \mathbf{x}_k to some $\mathbf{y} \in \mathbf{X}_{\text{goal}}^{(j)}$. Let XIT draw N i.i.d. samples from the mixture $q(\mathbf{x})$ defined in (14), and use the connection radius $r_N = \gamma(\log N/N)^{1/n}$ for γ above the mixture-aware RGG threshold and straight-line local connections with exact collision checking. Then

$$\lim_{N \rightarrow \infty} \Pr(XIT(N) \text{ finds a collision-free path } \sigma_N, \sigma_N(0) = \mathbf{x}_k, \sigma_N(1) = \mathbf{y}) = 1. \quad (15)$$

Proof: By the uniform-information mixture (14), the sampling density is bounded below, i.e., $q_I(\mathbf{x}) \geq \varepsilon/\lambda(\hat{\mathbf{X}}_f)$, so i.i.d. samples are dense with probability one [37, Ch. 5]. Let σ^* be a δ -clear path from \mathbf{x}_k to any $\mathbf{y} \in \mathbf{X}_{\text{goal}}^{(j)}$.

Set $\rho_N := r_N/4$ and cover σ^* with balls $B_i = \mathbb{B}(\mathbf{c}_i, \rho_N)$ whose centres satisfy $\|\mathbf{c}_{i+1} - \mathbf{c}_i\| \leq r_N/2$. Standard RGG connectivity/coverage results with $r_N = \gamma(\log N/N)^{1/n}$ [12] imply that, with probability approaching to one, each B_i contains at least one sample and any $\mathbf{x}_i \in B_i$, $\mathbf{x}_{i+1} \in B_{i+1}$ satisfy $\|\mathbf{x}_{i+1} - \mathbf{x}_i\| \leq 2\rho_N + \|\mathbf{c}_{i+1} - \mathbf{c}_i\| \leq r_N$, so the straight segment is an RGG edge and collision-free by clearance. Viewing XIT as a best-first search over this implicit RGG (as in a BIT* perspective [20]), and noting that it does not prune pre-solution and eventually accepts any collision-free cost-reducing edge, the entire edge chain to $\mathbf{X}_{\text{goal}}^{(j)}$ is inserted once it exists. Hence, the probability of XIT finds a collision-free path to $\mathbf{X}_{\text{goal}}^{(j)}$ tends to 1 as $N \rightarrow \infty$. ■

Note that when using the mixture distribution, the standard RGG threshold γ_{RGG} based on the uniform distribution should be augmented as $\gamma^* = \varepsilon^{-1/n} \gamma_{\text{RGG}}$. The above PC property can also be extended to all goal regions.

Assume the PC setup holds, the edges use the true additive cost as in (12) which is positive and Lipschitz in arc length, and the search uses admissible lower bounds, e.g., $\hat{c}(\mathbf{x}, \mathbf{y}) \leq c(\mathbf{x}, \mathbf{y})$ and $\hat{h}(\mathbf{x}) = \alpha \|\mathbf{x} - \mathbf{y}\|_2$, $\mathbf{y} \in \mathbf{X}_{\text{goal}}^{(j)}$, is less than true cost-to-go (i.e., distance-only bounds), we then have the following property.

Theorem 2 (Asymptotic optimality of XIT): Let $r_N = \gamma(\log N/N)^{1/n}$ with γ above the (mixture-aware) RGG threshold and use the admissible edge/goal heuristics above. For a sequence of runs of XIT with batch size $N \rightarrow \infty$, the best path cost in XIT’s tree (V_N, E_N) to any reachable goal region of non-zero measure converges almost surely to the optimal continuous value J_k^* :

$$\Pr\left(\lim_{N \rightarrow \infty} J_k(\sigma_N) = J_k^*\right) = 1,$$

where σ_N is XIT’s incumbent solution at batch size N .

Proof: The proof combines RGG approximation of optimal continuous paths as N grows with admissible best-first search that converges to the graph-optimal cost. Under $r_N = \gamma(\log N/N)^{1/n}$, the implicit RGG is asymptotically dense and admits δ -clear graph paths with cost arbitrarily close to J_k^* [12, Thm. 34]. With $\hat{c} \leq c$ and distance-only \hat{h} , XIT’s best-first expansion and rewiring over this RGG never overestimates future cost and monotonically reduces the

current path cost, mirroring the BIT* argument [20]. Hence, conditioned on the RGG event (which occurs with probability 1), $J_k(\sigma_N) \rightarrow J_k^*$ almost surely. ■

Remark 3: In this work, XIT is executed with a fixed batch of N samples per planning run. Consequently, within a single run it returns the best solution on the implicit RGG induced by that batch, but it is not “runtime asymptotically optimal” in the sense of improving unboundedly over time. Our AO statements are asymptotic in terms of the increasing batch size N . For time-critical active GDM applications, selecting the best path from a suitable fixed batch is adequate. As future work, XIT can be extended with progressive densification, in the spirit of BIT*, to obtain an anytime algorithm with almost-sure asymptotic optimality.

To demonstrate the asymptotic convergence of XIT, we present results from example scenarios in Figure 4. The trajectories in the left panel are generated by XIT based on the specified information field from the synthetic gas-polluted datasets, cost function, and heuristic setup. The empirical convergence results with respect to the sample size N for each of these scenarios averaged over 10 simulation runs are also included in the right panel.

V. GAS FRONTIER DETECTION

As introduced in Section III-B, gas frontiers $\mathcal{F}_k^{\text{gas}}$ are intended to identify the boundary of high concentration regions that remain adjacent to unobserved gas states. They complement conventional occupancy frontiers $\mathcal{F}_k^{\text{occ}}$ by steering the robot toward plume boundaries rather than only the edge of the known geometric map. Figure 5 illustrates this concept in isolation of $\mathcal{F}_k^{\text{occ}}$, showing both the cell-level depiction and the resulting gas exploration behaviour as gas frontiers guide the robot to probe unresolved plume boundaries. We present the Wavefront Gas Frontier Detection (WGFD) algorithm to detect them. The proposed gas edge detection algorithm is based on wavefront frontier detection (WFD), an iterative method introduced in [35] that conducts a graph search over known free-space regions of an occupancy grid map to identify frontiers. Frontier algorithms relying on raw sensor readings, such as FFD [35], are not suitable for gas frontier detection, since the *in situ* gas sensor utilised provides point measurements that cannot directly infer gas frontiers but can be processed into a gas distribution map. WGFD applies the same wavefront principles as WFD to identify unknown cells that lie adjacent to observed regions with high gas concentration.

A. Formal Definition of Gas Frontiers

We first formalise the notion of a gas frontier cell at a fixed planning step k and, following the convention in Section IV-A, drop the index k on all quantities where this causes no ambiguity. Recall that the occupancy grid \mathcal{M}^{occ} is defined on the lattice \mathcal{C} , and that the known free subset $\mathcal{X}_{\text{free}}$ in (1) corresponds to the union of cells whose occupancy probability is below the free threshold τ_{free} . At the level of individual cells, we define the set of free cells as

$$\mathcal{C}^{\text{free}} := \{c \in \mathcal{C} \mid p(c) \leq \tau_{\text{free}}\}. \quad (16)$$

The gas distribution map \mathcal{M}^{gas} provides the posterior mean $\mu(c)$ and variance $\varepsilon(c)$ for each free cell $c \in \mathcal{C}^{\text{free}}$, obtained from the GMRF inference described in Section III-A. Let $\mathcal{C}_{\text{gas,obs}} \subseteq \mathcal{C}^{\text{free}}$ denote the subset of cells whose gas state has been sufficiently constrained by measurements, and let

$$\mathcal{C}_{\text{gas,unk}} := \mathcal{C}^{\text{free}} \setminus \mathcal{C}_{\text{gas,obs}}$$

denote the free cells whose gas state remains unobserved or highly uncertain. The precise definition of $\mathcal{C}_{\text{gas,obs}}$ is determined by the inference procedure; for example, it may consist of cells whose marginal variance $\varepsilon(c)$ is below a variance threshold. For the purposes of this work, it is sufficient that $\mathcal{C}_{\text{gas,obs}}$ and $\mathcal{C}_{\text{gas,unk}}$ form a partition of $\mathcal{C}^{\text{free}}$.

To identify gas frontiers we require a gas concentration threshold that selects cells belonging to significant gas regions. We define a dynamic threshold τ_{gas} as

$$\tau_{\text{gas}} := \max(q_p, \tau_{\text{gas,min}}), \quad (17)$$

where q_p is the p th percentile of the posterior mean values $\mu(c)$ over $\mathcal{C}_{\text{gas,obs}}$, and $\tau_{\text{gas,min}} > 0$ is a user specified lower bound that prevents overly permissive detection in near zero gas conditions. A free cell $c \in \mathcal{C}_{\text{gas,obs}}$ is said to be gas critical if

$$\mu(c) \geq \tau_{\text{gas}}, \quad (18)$$

and the set of gas critical cells is denoted

$$\mathcal{C}^{\text{crit}} := \{c \in \mathcal{C}_{\text{gas,obs}} \mid \mu(c) \geq \tau_{\text{gas}}\}. \quad (19)$$

We adopt a neighbourhood operator $\mathcal{N}(c) \subset \mathcal{C}$, which returns the set of cells adjacent to c on the lattice. A cell $c \in \mathcal{C}_{\text{gas,unk}}$ is classified as a gas frontier cell if it lies in the unknown gas region yet is adjacent to at least one gas critical cell, that is,

$$c \in \mathcal{C}_{\text{gas,unk}} \text{ is a gas frontier cell if } \mathcal{N}(c) \cap \mathcal{C}^{\text{crit}} \neq \emptyset. \quad (20)$$

The set of all gas frontier cells is written

$$\mathcal{C}^{\text{gf}} := \{c \in \mathcal{C}_{\text{gas,unk}} \mid \mathcal{N}(c) \cap \mathcal{C}^{\text{crit}} \neq \emptyset\}. \quad (21)$$

A gas frontier f^{gas} is defined as a maximal connected subset of \mathcal{C}^{gf} under the neighbourhood relation, meaning that any two cells in f^{gas} can be joined by a path of neighbouring gas frontier cells and no strict superset of f^{gas} has this property. The collection of all gas frontiers at the current planning step is written

$$\mathcal{F}^{\text{gas}} := \{f_1^{\text{gas}}, f_2^{\text{gas}}, \dots, f_M^{\text{gas}}\}, \quad (22)$$

which corresponds to the set $\mathcal{F}_k^{\text{gas}}$ introduced in Section III-B once the index k is reinstated. Each $f_m^{\text{gas}} \in \mathcal{F}^{\text{gas}}$ captures the boundary of a high concentration gas region that is adjacent to unknown gas states (Fig. 5). These clusters provide the gas frontier component of the frontier based goal set \mathcal{G}_k that drives plume aware exploration in the active GDM framework.

B. Wavefront Gas Frontier Detection

The algorithm begins by initialising the gas frontier set \mathcal{F}^{gas} as empty and identifying the cell $c_r \in \mathcal{C}^{\text{free}}$ that contains the robot’s current pose \mathbf{x}_k (Alg. 2, Lines 1-2). The graph search proceeds only if the robot is located within a gas critical region. If the posterior mean at c_r does not reach

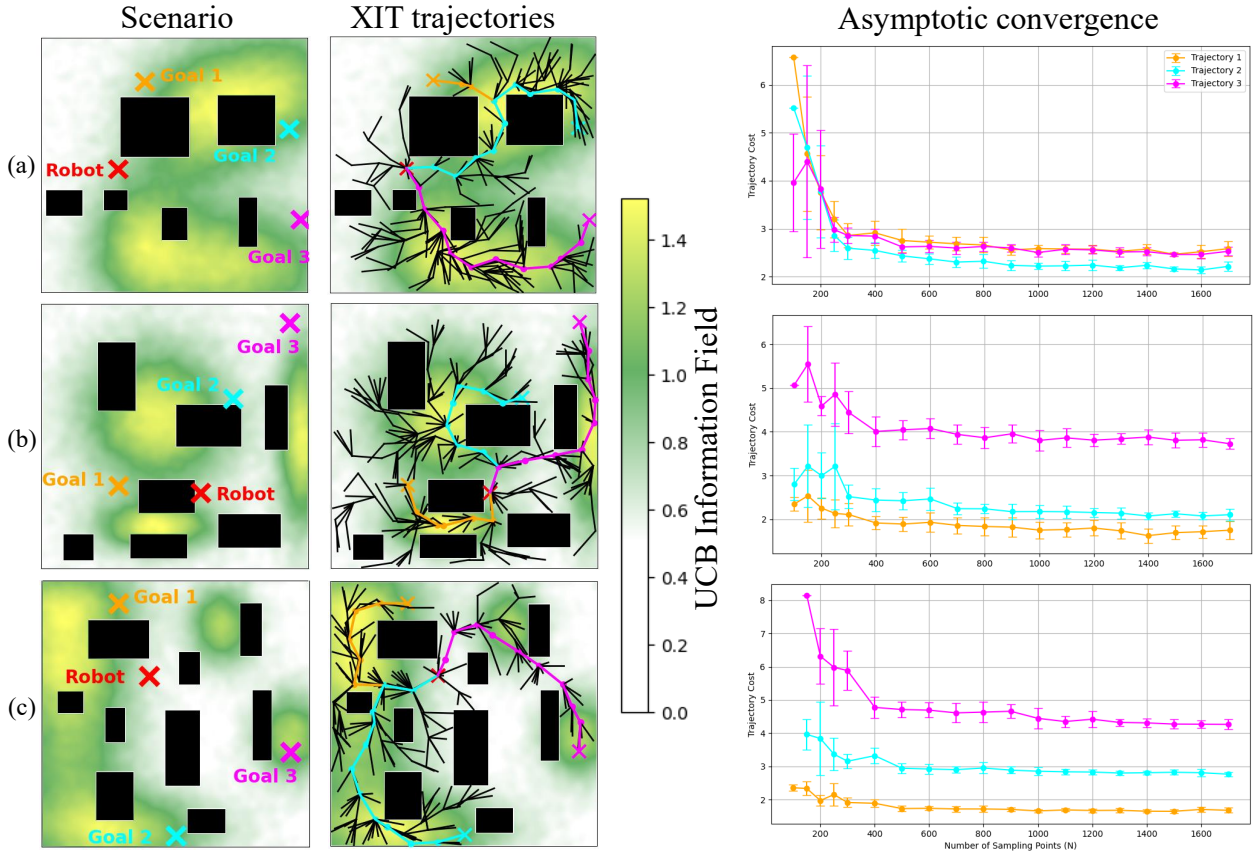


Fig. 4. Example trajectories generated by XIT in three synthetic scenarios using the information field, cost function, and heuristic setup described in Section IV-C. For the illustrative trajectories, $N = 300$ was used. The right-hand side of each example shows the corresponding asymptotic convergence results over ten simulations for each N .

the threshold, $\mu(c_r) < \tau_{\text{gas}}$, then no local plume boundary is considered relevant and the algorithm returns the empty frontier set (Alg. 2, Lines 3-4). Otherwise, the gas frontier flags ϕ_{gf} and visited flags ϕ_v are initialised for all cells, the robot cell c_r is marked visited, and the outer breadth-first search (BFS) queue Q is initialised with c_r (Alg. 2, Lines 5:7).

The outer BFS propagates only through the connected component of $\mathcal{C}^{\text{crit}}$ that contains the robot's current cell (Alg. 2, Lines 8:26). Although $\mathcal{C}^{\text{crit}}$ denotes the set of all gas-critical cells in the map, the wavefront cannot cross subcritical regions, so only the local gas region is explored. At each iteration, the next cell c is dequeued from Q and its neighbours $c_n \in \mathcal{N}(c)$ are examined (Alg. 2, Line 9). If a neighbour satisfies the new gas frontier predicate in Alg. 3, it is immediately flagged as a gas frontier cell, used to initialise a new frontier set f^{gas} , and enqueued into an inner BFS queue Q_f (Alg. 2, Lines 11:14). The inner BFS then groups all connected gas frontier cells into the same frontier (Alg. 2, Lines 15:21): while Q_f is not empty, the current cell c' is dequeued, its neighbours c'_n are checked, and any neighbour that again qualifies as a new gas frontier cell is flagged, added to f^{gas} , and enqueued into Q_f . This inner loop terminates once no further neighbouring gas frontier cells can be found, yielding a maximal connected subset $f^{\text{gas}} \subset \mathcal{C}^{\text{gf}}$ in the sense of the formal definition. Frontiers whose cardinality falls below a minimum size threshold are discarded, filtering out small, noise induced structures (Alg. 2,

Lines 22–23).

If a neighbour c_n is not a gas frontier cell but belongs to the gas critical set $\mathcal{C}^{\text{crit}}$ being explored and has not yet been visited, it is marked visited and enqueued into the outer BFS queue Q (Alg. 2, Lines 24:26). In this way, the outer BFS explores the interior of the gas region above the threshold, while the inner BFS extracts the plume boundary where this region borders unknown gas states.

The helper function in Alg. 3 implements the cell level definition in Eq. (20). A candidate cell c must lie in the gas unknown set $\mathcal{C}^{\text{gas,unk}}$, must not already have been assigned to an existing frontier, and must have at least one neighbouring cell in the gas critical set $\mathcal{C}^{\text{crit}}$. Cells that violate any of these conditions are rejected. When the outer BFS queue Q becomes empty, all reachable gas critical regions have been processed and the procedure returns \mathcal{F}^{gas} .

VI. SIMULATION STUDY

While no established benchmark exists for active GDM in unknown, cluttered environments, this section evaluates the proposed XIT planner within our active GDM framework (Fig. 2). We perform high-fidelity Monte Carlo simulation in Robot Operating System (ROS), with the GADEN simulator [38] providing realistic gas dispersion within the environment. Performance is reported relative to an RRT* frontier-exploration baseline, and we then examine the influence of

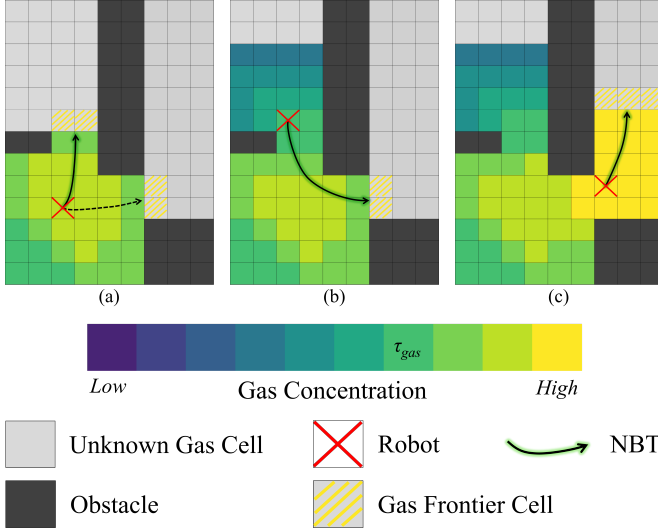


Fig. 5. Cell-level depiction of gas frontiers and their role in path planning within an active GDM task over three sequential time steps. (a) The robot enters from the bottom left and finds itself within a critical gas region above τ_{gas} based on its updated belief. Two gas frontiers are identified, and one is selected as the NBT. (b) Upon reaching the gas frontier, the updated belief reveals that the area is no longer a priority as no new gas frontiers emerged based on the estimate, suggesting a less concentrated region. It now targets the other previously identified gas frontier from (a), which has remained unresolved. (c) Resolving the second gas frontier reveals a high-concentration zone that generates new a new gas frontier, which can be explored next to continue the adaptive plume probing process.

XIT’s key design choices, namely goal-selection policy and cost formulation, using representative limiting cases of the proposed UCB-distance cost.

A. Simulation Setup

The simulation scenario comprises a cluttered industrial-style environment with storage containers and partitioned rooms, as shown in Fig. 6. To demonstrate the capabilities of XIT in complex multi-source gas mapping scenarios, three acetone sources were placed at distinct locations with varying release rates detailed in Table I. The filament growth rate in GADEN was set to $15 \text{ cm}^2/\text{s}$ for all sources with a steady 3 m/s wind field (light breeze conditions). Although GADEN models source releases as unsteady processes, the steady wind field imposes a consistent advection regime and ensures approximately time-invariant plume structures, which is essential for fair comparison across trials.

The simulated mobile platform travelled at 1.25 m/s and was equipped with a PID sensor sampling at 2 Hz for gas detection and a standard LiDAR for range measurements. Online occupancy mapping was performed using the open-source SLAM Toolbox [39], with obstacles inflated by approximately 0.2 m to ensure robust planning. To isolate planning performance, true localisation was obtained directly from Gazebo and path following was idealised such that the robot tracked planned trajectories perfectly, deliberately eliminating variance from robot dynamics and control errors that would otherwise obscure differences in the planning metrics.

The GMRF [3] was used as the GDM function with the GBP solver from [8] to achieve real-time updates. Conven-

Algorithm 2: WGFD($\mathcal{M}^{\text{gas}}, \mathcal{M}^{\text{occ}}, \mathbf{x}_k, \tau_{\text{gas}}$)

```

1  $\mathcal{F}^{\text{gas}} \leftarrow \emptyset;$ 
2  $c_r \leftarrow c(\mathbf{x}_k);$ 
3 if  $\mu(c_r) < \tau_{\text{gas}}$  then
4   return  $\mathcal{F}^{\text{gas}}$ 
5  $\phi_{\text{gf}}(c), \phi_v(c) \leftarrow \text{False for all } c \in \mathcal{C};$ 
6  $\phi_v(c_r) \leftarrow \text{True};$ 
7 Initialise BFS queue  $Q$  with  $c_r$ ;
8 while  $Q \neq \emptyset$  do
9    $c \leftarrow \text{dequeue}(Q);$ 
10  foreach  $c_n \in \mathcal{N}(c)$  do
11    if  $\text{isNewGasFrontierCell}(c_n)$  then
12       $\phi_{\text{gf}}(c_n) \leftarrow \text{True};$ 
13       $f^{\text{gas}} \leftarrow \{c_n\};$ 
14      Initialise BFS queue  $Q_f$  with  $c_n$ ;
15      while  $Q_f \neq \emptyset$  do
16         $c' \leftarrow \text{dequeue}(Q_f);$ 
17        foreach  $c'_n \in \mathcal{N}(c')$  do
18          if  $\text{isNewGasFrontierCell}(c'_n)$  then
19             $\phi_{\text{gf}}(c'_n) \leftarrow \text{True};$ 
20             $f^{\text{gas}} \leftarrow f^{\text{gas}} \cup \{c'_n\};$ 
21            enqueue( $c'_n, Q_f$ );
22        if  $|f^{\text{gas}}| \geq \text{min\_frontier\_size}$  then
23           $\mathcal{F}^{\text{gas}} \leftarrow \mathcal{F}^{\text{gas}} \cup \{f^{\text{gas}}\};$ 
24      else if  $c_n \in \mathcal{C}^{\text{crit}}$  and  $\phi_v(c_n) = \text{False}$  then
25         $\phi_v(c_n) \leftarrow \text{True};$ 
26        enqueue( $c_n, Q$ );
27 return  $\mathcal{F}^{\text{gas}}$ 

```

Algorithm 3: isNewGasFrontierCell(c)

```

1 if  $c \notin \mathcal{C}^{\text{gas,unk}}$  then
2   return  $\text{False}$ ; // Gas state is not
   unknown
3 if  $\phi_{\text{gf}}(c) = \text{True}$  then
4   return  $\text{False}$ ; // Already flagged as gas
   frontier
5 if  $\mathcal{N}(c) \cap \mathcal{C}^{\text{crit}} = \emptyset$  then
6   return  $\text{False}$ ; // No neighbouring gas
   critical cell
7 return  $\text{True}$ 

```

tional frontier detection was implemented using the WFD algorithm [35], while gas frontiers were identified using the proposed WGFD algorithm (Section V). Table I summarises the key simulation parameters.

B. Evaluation Methodology

The XIT planner was configured with a batch size of $N = 300$ samples per planning iteration. At each iteration, up to five goal regions were selected based on the goal-selection

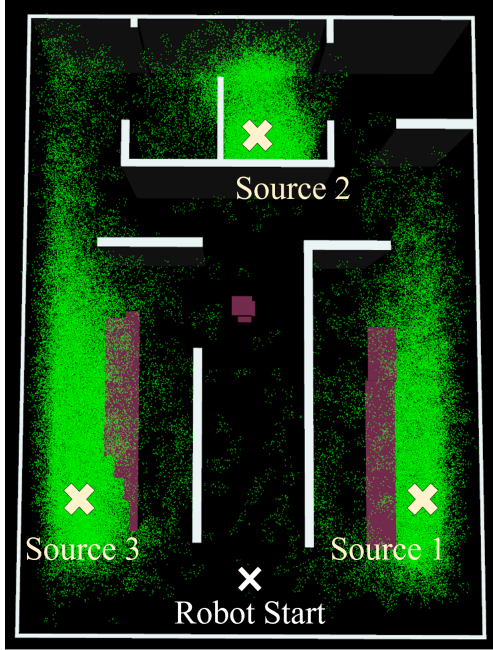


Fig. 6. High-fidelity simulation scenario featuring a cluttered, industrial indoor layout with multi-source acetone dispersion. White lines denote walls, and magenta blocks denote storage containers (both obstacles). Green particles visualise the dispersion field. Crosses indicate the three acetone sources and the robot start, which are labelled accordingly.

TABLE I
KEY SIMULATION PARAMETERS.

Parameter	Value
Environment & Gas Sources	
Environment size	16 m \times 20 m
Source 1/2/3 release rates	1750/1250/1000 ppm/s
Filament growth rate	15 cm ² /s
Wind field	3 m/s (steady)
Robot Configuration & Sensing	
Speed	1.25 m/s
Obstacle inflation	0.2 m
PID sensor sampling rate	2 Hz
GMRF Hyperparameters	
Lattice resolution	0.1 m
Regularisation variance (σ_r^2)	3
Observation variance (σ_s^2)	10
Time-decay variance (σ_t^2)	1×10^{10}
Default factor variance (σ_d^2)	0.001
Gas Frontiers	
Critical gas threshold Eq. (17)	$\tau_{\text{gas,min}} = 2 \text{ ppm}$, $q_p = 10$

policy. For each selected goal region $f \in \mathcal{F}_k^{\text{occ}} \cup \mathcal{F}_k^{\text{gas}}$, the goal set $\mathbf{X}_{\text{goal}}^{(j)}$ was constructed using the $k_n = 3$ nearest samples from \mathbf{X}_s to the frontier centroid. A small uniform distribution component (20%) was added to the informed UCB sampling distribution (Eq. 8) to ensure coverage of the entire free space, as described in Section IV-D. All simulations were executed on an AMD Ryzen 9 5950X 16-Core Processor, with XIT achieving an average planning time of 0.74 s per iteration, enabling real-time operation. Table II provides a summary of the key XIT configuration parameters.

Three XIT goal-selection policies are tested. *XIT-F* selects up to 5 occupancy frontiers at random. *XIT-FGF* queues all

TABLE II
XIT PLANNER CONFIGURATION PARAMETERS.

Parameter	Value
Batch size (N)	300 samples
Maximum goal regions	5
Nearest samples per goal (k_n)	3
Uniform sampling component	20%

available occupancy frontiers first (randomly selecting 5 if more exist), then fills remaining slots with random gas frontiers. *XIT-GFF* reverses this: gas frontiers first, then occupancy frontiers fill remaining slots.

Two cost formulations are evaluated: *UCB*, the proposed information penalty cost at $\alpha = 0$ for both tree expansion (Eq. (12)) and trajectory selection (Eq. (13)), representing gas exploitation planning, and *Euclidean*, distance-only cost for tree expansion. XIT-GFF and XIT-FGF are each evaluated under both cost formulations. Performance is benchmarked against *RRT* Frontier Exploration*, which uses RRT* with distance-based cost to plan paths to occupancy frontiers, representing standard frontier-based exploration without gas-awareness. Note that XIT-F with Euclidean cost would yield similar performance to this baseline at the scale of this active GDM experiment due to the absence of gas-awareness in both approaches, and is therefore not separately evaluated. XIT-F with UCB cost is included, yielding five total XIT configurations plus the baseline.

Each trial began with the robot at a fixed starting location in an initially unknown environment and ran for a fixed duration of 5 minutes to endure consistent conditions for comparing the different algorithm configurations. To reduce variance, 20 Monte Carlo simulations were conducted for each configuration, with performance averaged across trials.

System performance was evaluated using three metrics. The first two assess GDM quality in critical gas regions, defined for evaluation purposes as free-space cells where ground truth concentration exceeds $z_{\text{thresh}} = 2.5 \text{ ppm}$. These critical regions, corresponding to areas of significant acetone presence, are visualised spatially in Fig. 9 (outlined in red). This focus on critical regions is particularly important for entropy evaluation, as computing entropy across the entire map would primarily reflect the number of measurements obtained in newly explored areas rather than the quality of gas distribution inference. The metrics are: (i) root mean square error (RMSE), measuring mapping accuracy against ground truth obtained from a fine lawnmower sweep; and (ii) total differential entropy, quantifying total uncertainty in the gas distribution estimate within these highly concentrated areas. The third metric measures exploration completeness, defined as the rate at which the occupancy grid map approaches full coverage over time. Final performance is reported as percentage improvement relative to the RRT* Frontier Exploration baseline.

The GDM RMSE at planning step k is computed as

$$\text{RMSE}_k = \sqrt{\frac{1}{|\mathcal{X}_{\text{crit}}|} \sum_{\mathbf{x} \in \mathcal{X}_{\text{crit}}} [\hat{\mu}_k(\mathbf{x}) - \mu_{\text{GT}}(\mathbf{x})]^2}, \quad (23)$$

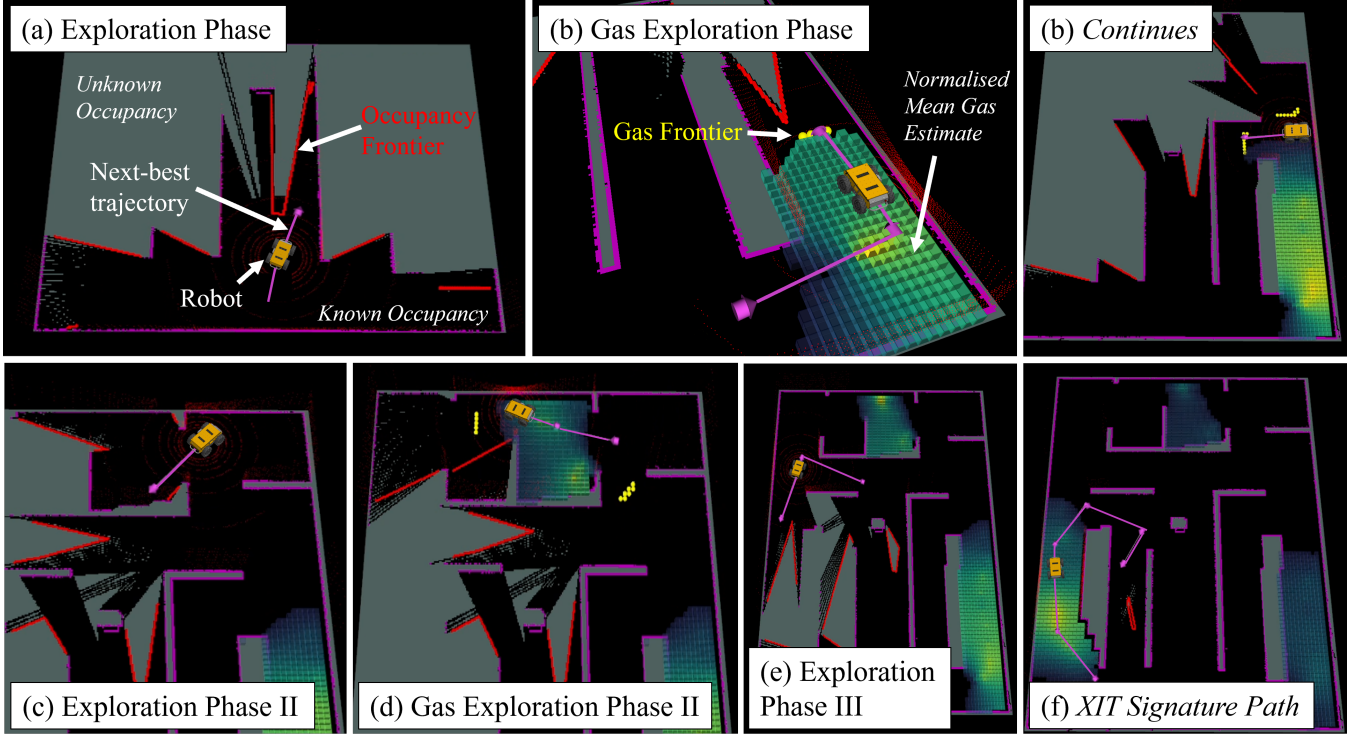


Fig. 7. Illustrative run of the active GDM process in simulation using XIT-GFF with UCB cost. Only the selected NBT is shown in each phase for clarity. The normalised posterior mean gas estimate is overlaid using the viridis colormap (yellow indicates higher concentration). (a) Initial structural exploration with occupancy frontiers. (b) Gas frontier detection triggers targeted probing of critical gas boundaries. (c–e) Alternation between occupancy exploration and gas-structure exploration as new critical regions are encountered. (f) Example of a gas-exploitative path that traverses high-concentration regions rather than taking the shortest route.

where $\hat{\mu}_k(\mathbf{x})$ is the estimated gas concentration at state \mathbf{x} , $\mu_{\text{GT}}(\mathbf{x})$ is the ground truth concentration, and $\mathcal{X}_{\text{crit}} = \{\mathbf{x} \in \mathcal{X}_{\text{free}} \mid \mu_{\text{GT}}(\mathbf{x}) > z_{\text{thresh}}\}$ is the set of critical gas region cells.

The total differential entropy in critical gas regions at step k is calculated as

$$H_k = \sum_{\mathbf{x} \in \mathcal{X}_{\text{crit}}} \frac{1}{2} \log (2\pi e \varepsilon_k(\mathbf{x})), \quad (24)$$

where $\varepsilon_k(\mathbf{x})$ is the marginal posterior variance from the GMRF at cell \mathbf{x} .

The occupancy map completeness is defined as the fraction of the true free space $\mathcal{X}_{\text{free}}$ that has been identified in the known-free subset $\hat{\mathcal{X}}_{\text{free}}(k)$ (Eq. (1)).

C. Results

Figure 7 illustrates a representative run of the XIT-GFF configuration with the UCB cost, demonstrating the natural alternation between structural exploration and gas-specific probing and exploitation. Initially, the robot explores the environment using occupancy frontiers. Upon encountering critical gas regions, gas frontiers are detected and prioritised due to the policy, leading the robot to probe the boundaries of the critical gas structure it finds itself in. Once local gas structure is resolved, the system returns to occupancy exploration. As the gas map becomes fairly populated, UCB-driven gas-exploitative paths towards these goals become more significant, as seen in Fig. 7f, creating an adaptive exploration and exploitation process.

Figure 8 presents the temporal evolution of all three metrics averaged over 20 Monte Carlo simulations for each configuration. The UCB information penalty cost function consistently outperformed the Euclidean cost in gas mapping quality (RMSE and entropy) for the same goal-selection policy, while achieving comparable exploration efficiency.

The RMSE plot (Fig. 8, top) shows that XIT-GFF with UCB cost achieves the greatest reduction in mapping error, reaching below 15 ppm by the end of the mission; this represents a 25.5% improvement over the RRT* Frontier Exploration baseline (see Table III for detailed metrics). This spatial reduction in error is visualized in Fig. 9, which shows the per-cell RMSE distribution at three time points. The critical gas regions (outlined in red) demonstrate that XIT-GFF more effectively reduces error in and around these regions compared to the baseline, particularly in the later stages of the mission ($150 \text{ s} < t < 300 \text{ s}$), with some residual error near walls due to obstacle inflation constraints preventing the robot from sampling directly adjacent to these surfaces. The entropy plot (Fig. 8, middle) demonstrates similar trends, with XIT-GFF using UCB cost achieving 23.7% lower entropy in critical regions. Map completeness (Fig. 8, bottom) shows similar final coverage across all methods, with all variants reaching near-complete coverage by the halfway mark, indicating that the gas-frontier mechanism does not compromise exploration efficiency. The primary performance differences lie in gas mapping quality (RMSE and entropy) rather than spatial coverage.

TABLE III
FINAL GDM PERFORMANCE AT $T = 300$ s (MEAN \pm STD OVER 20 TRIALS).

Method	Cost	RMSE_T [ppm]	RMSE Reduction [%]	H_T	Entropy Reduction [%]
RRT* Frontier Exploration	Euclidean	20.0 ± 4.4	0.0	1254 ± 244	0.0
XIT-F	UCB	17.2 ± 3.1	14.1	1088 ± 280	13.2
XIT-FGF	Euclidean	19.1 ± 3.5	4.7	1169 ± 245	6.8
XIT-FGF	UCB	17.9 ± 4.7	10.5	1022 ± 217	18.5
XIT-GFF	Euclidean	18.3 ± 4.4	8.8	1096 ± 263	12.6
XIT-GFF	UCB	14.9 ± 1.9	25.5	957 ± 169	23.7

Percentage reductions computed relative to RRT* Frontier Exploration baseline.

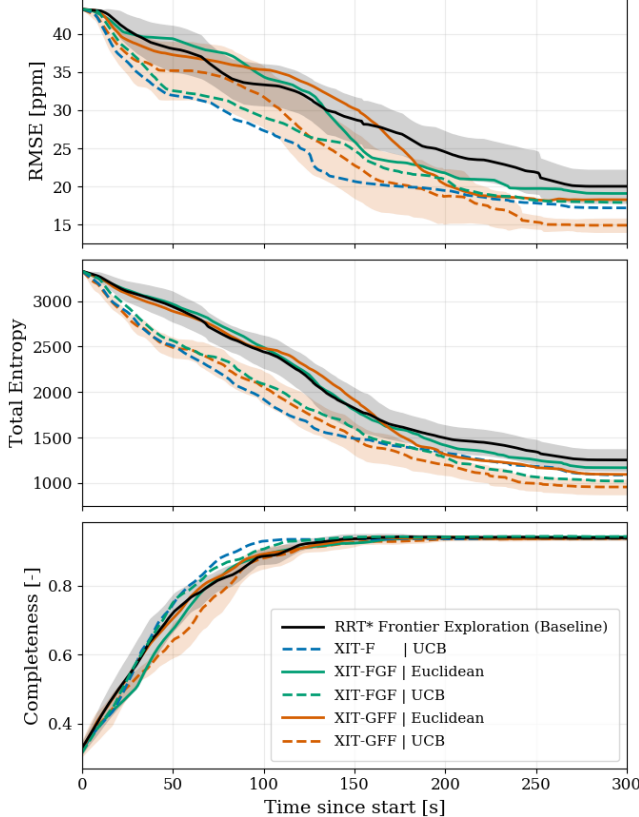


Fig. 8. Performance comparison over time in terms of RMSE (top), total differential entropy (middle), and map completeness (bottom), for different goal-selection policies and cost formulations. Shaded regions indicate 95% confidence intervals for XIT-GFF with UCB (best performing) and RRT* Frontier Exploration (baseline).

In all XIT policies, at the start of each run when no gas frontiers exist, occupancy frontiers are automatically prioritised, initiating the environmental exploration phase as illustrated in Fig. 7. Among the goal-selection policies, queuing gas frontiers first followed by occupancy frontiers (XIT-GFF) proved most effective. This result is intuitive: prioritising gas frontiers encourages the robot to thoroughly explore known gas regions before moving to new areas where gas may or may not be present. The gas frontier mechanism provides a structured approach to this, as probed frontiers are removed once local gas structure is resolved, naturally guiding the robot away from already-explored gas regions. This contrasts with concentration-based or uncertainty-based methods, which can exhibit suboptimal looping by revisiting high-concentration or high-variance cells without clear termination criteria, as

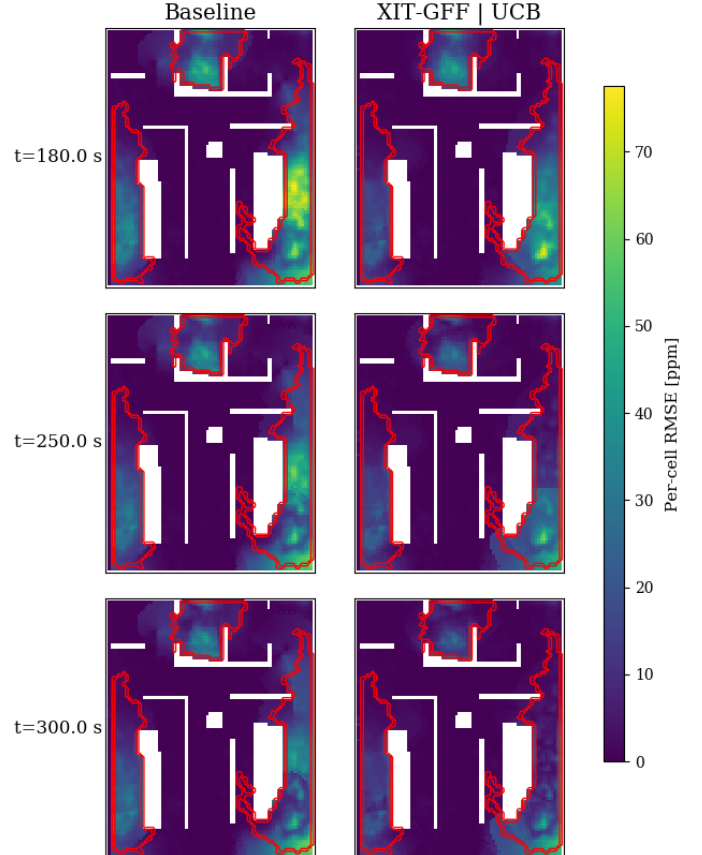


Fig. 9. Per-cell RMSE maps over time for RRT* Frontier Exploration baseline and XIT-GFF (mean over trials). White regions are obstacles. The colour scale indicates RMSE in ppm. Critical regions used in the RMSE and entropy calculations are outlined in red for spatial recognition.

observed in [28]. While [28] addressed this by discretising the space with K-means clustering and adaptively sampling within predefined clusters in obstacle-free environments, our approach must simultaneously explore an unknown environment while mapping gas. We integrate occupancy frontiers for structural exploration with gas frontiers for targeted probing, where the UCB cost function drives gas-exploitative paths and the system naturally transitions between objectives based on emerging critical gas regions rather than predefined spatial partitions. Between the other XIT policies, XIT-FGF prioritises occupancy frontiers first, emphasising a more exploration-focused approach that may delay thorough investigation of known gas structures. Notably, in both policies, when both gas frontiers and occupancy frontiers are in the queue, the most

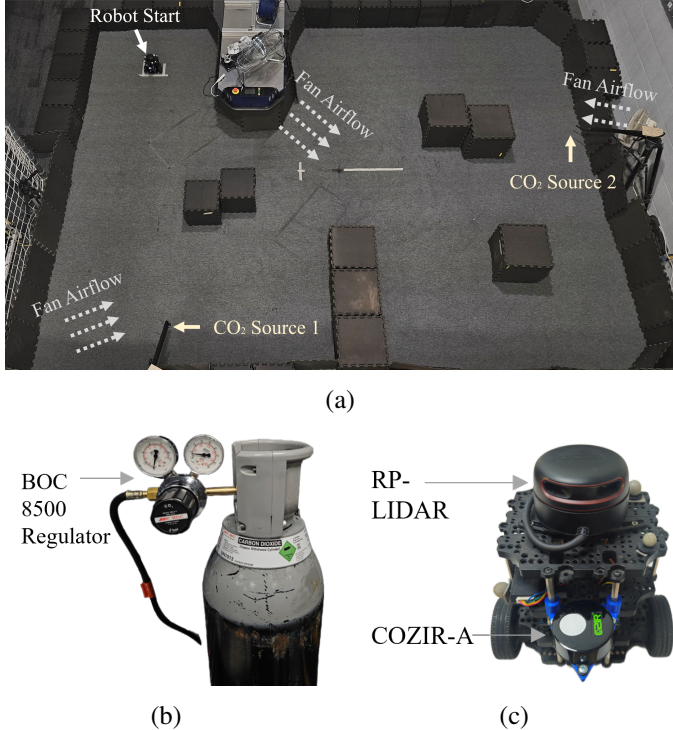


Fig. 10. Experimental setup. (a) Top-down view of the 5.0 m \times 3.7 m arena showing airflow directions from fans (dashed arrows) and CO₂ release nozzles (Source 1 and Source 2). Note that the two fans on the left are more powerful than the single and smaller fan on the right, creating asymmetric dispersion patterns. (b) BOC 8500 regulator attached to the pressurised CO₂ cylinder used for controlled gas release. (c) TurtleBot3 platform equipped with a COZIR-A CO₂ sensor and RP-LiDAR for gas mapping and navigation.

gas-exploitative trajectory is identified via the UCB trajectory selection function (Eq. (13)). It was observed that this often favours trajectories to gas frontiers due to the higher UCB density between the robot and these boundaries, which likely explains why XIT-FGF with UCB cost achieves the second-best entropy reduction in critical regions, outperforming XIT-F with UCB cost which does not consider gas frontiers as a goal source.

Table III summarises the final performance metrics at $T = 300$ s, confirming that XIT-GFF with UCB cost achieves the best performance with low variability across trials.

VII. EXPERIMENTAL TRIAL

A physical experiment was conducted to validate the proposed XIT planner and broader active GDM framework (Fig. 2) in a scaled indoor environment (Fig. 10) designed to emulate a confined gas-leak scenario. The arena measured 5.0 m \times 3.7 m and was enclosed with barriers to mimic the restricted airflow of an indoor space. Two CO₂ sources were installed at opposite sides of the arena, each connected to a pressurised CO₂ cylinder via a BOC Series 8500 multi-stage regulator (Fig. 10b). CO₂ was selected as the tracer gas due to its density being greater than that of air, which causes it to settle near ground level, creating realistic stratification in the scaled environment. Three fans generated controlled airflow to produce a complex, multi-region gas plume pattern

that challenged the planner's ability to identify and exploit informative regions.

The mobile platform was a TurtleBot3 (Fig. 10c) equipped with a COZIR-A infrared CO₂ sensor mounted at 0.15 m height to sample near the gas layer. The robot travelled at 0.15 m/s with obstacle inflation of 0.2 m for safe navigation. A Vicon motion-capture system provided high-accuracy odometry, while the occupancy grid map was generated online using SLAM Toolbox [39] and gas distribution mapping was performed by GMRF [3] with the GBP solver [8], as in the simulation study. Path following employed a simple proportional controller that maintains constant forward velocity while adjusting angular velocity based on heading error to the next waypoint. Due to the slow response of the COZIR-A sensor, the robot executed a stop-and-sample routine at each vertex of the NBT, remaining stationary for 5 s to ensure reliable readings. This contrasts with the faster acetone (PID) sensor used in the simulation study, where continuous sensing was possible.

The experiment employed XIT-GFF with the UCB cost function ($\alpha = 0$) for both tree expansion (Eq. (12)) and trajectory selection (Eq. (13)), the most successful configuration from simulation, with up to five candidate goal regions evaluated per planning iteration. A fixed threshold $\tau_{\text{gas}} = 600$ ppm was used in place of the dynamic threshold (Eq. (17)) due to the limited spatial extent of the scaled environment and the slow response characteristics of available CO₂ sensors when detecting concentration changes in the range just above ambient background levels (approximately 400 ppm). The experiment started 30 s after initiating gas release to allow plume formation and continued for approximately eleven minutes. Once all frontiers and gas frontiers were resolved, XIT entered a fallback mode in which goals were sampled randomly in free space. The run terminated after two consecutive XIT trajectories failed to reveal any new frontiers or gas frontiers.

During the run, the robot began in an unknown region outside the gas plume and initially navigated toward frontiers to build the occupancy map, as shown at the top of Fig. 11. As the robot approached the first source, gas frontiers were established, prompting XIT to probe the local gas boundaries around the source. The robot then transitioned to an exploration phase that led it near the second source, where a subsequent gas-exploration phase occurred within a more complex dispersion region (Fig. 11, middle row). Throughout the experiment, XIT generated trajectories through high-UCB areas, often gas-exploitative regions, ensuring that high-concentration zones were revisited when possible. An example of this behaviour is shown in the bottom row of Fig. 11, where the robot passes through both regions downwind of the sources on its way to the final goal. The final gas map (Fig. 12) showed CO₂ levels exceeding 2000 ppm in some regions, forming extended gas zones with higher concentrations near the release points. Notably, higher concentrations are observed near Source 2 on the right side of the arena, consistent with the asymmetric airflow pattern created by the two more powerful fans on the left side directing flow toward this region.

VIII. CONCLUSION

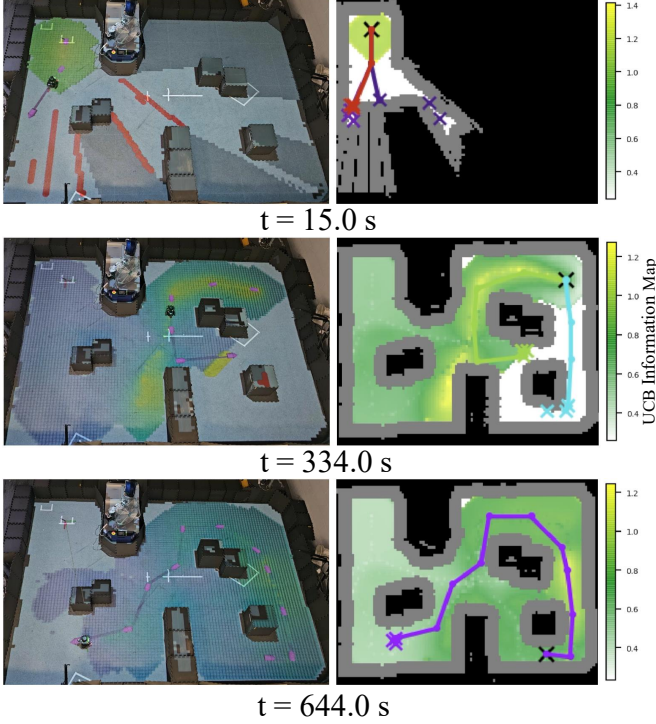


Fig. 11. Progression of the real-world experiment using the proposed XIT planner in the scaled indoor gas-leak environment. Each row shows the top-down view of the arena (left) with the normalised gas mean map projected on the floor, where red, yellow, and purple lines indicate frontiers, gas frontiers, and the NBT, respectively. The corresponding XIT paths and UCB information field are shown on the right with obstacle inflation in grey. From top to bottom: XIT begins in a pure exploration phase, as the starting location lies outside the critical gas region, proceeds through gas-exploration phases around both sources (the second shown in the middle), and concludes with a final gas-exploitative trajectory that passes downwind through both gas regions toward the goal. A video of the experiment is available [here](#).

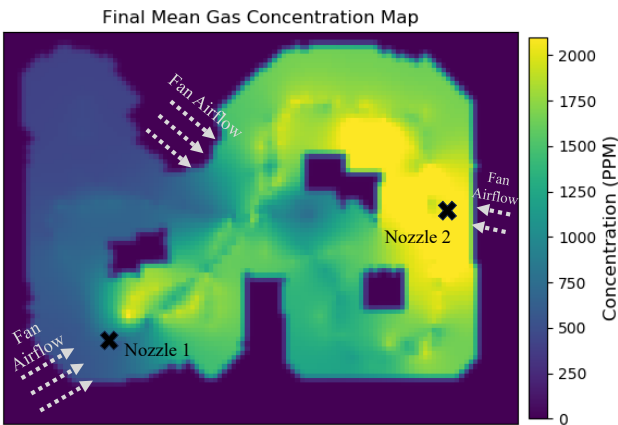


Fig. 12. Final mean gas concentration map obtained in the real-world experiment using the proposed XIT planner within our proposed active GDM framework (Fig. 2). Source locations and airflow directions (dashed arrows) are indicated as in Fig. 10a.

This paper presents a novel active GDM framework for unknown, cluttered environments, where a robot must simultaneously reason about environmental exploration, structural mapping, and gas dispersion inference. At the core of this framework is XIT, a sampling-based IPP planner that addresses these objectives through: (i) occupancy frontiers for environmental exploration, (ii) gas frontiers, boundaries of critical regions adjacent to unobserved states detected by the proposed WGFD algorithm, for gas structure exploration, and (iii) UCB-guided tree expansion that favours high-concentration, high-uncertainty regions for gas exploitation. We establish theoretical properties of XIT, proving probabilistic completeness and asymptotic optimality, and demonstrate empirical convergence in synthetic scenarios.

High-fidelity Monte Carlo simulation validates the effectiveness of the proposed framework. The UCB-based cost function consistently outperforms distance-based planning in gas mapping quality (RMSE and entropy) while maintaining comparable coverage efficiency. Among the XIT goal-selection policies tested, prioritising the queuing of gas frontier over occupancy frontiers (XIT-GFF) proves most effective, achieving 25.5% reduction in RMSE and 23.7% reduction in entropy compared to a standard RRT* frontier exploration baseline. The introduction of gas frontiers provides an intuitive and natural mechanism for gas structure exploration. As probed frontiers are removed once local gas structure is resolved, the robot is naturally guided away from already-explored gas regions toward unknown areas which may contain critical gas. This inherently prevents the suboptimal looping behaviour observed in concentration-based or uncertainty-based methods, which can revisit high-concentration or high-variance cells without clear or natural termination criteria. Combined with occupancy frontiers for structural exploration and the UCB cost function for gas-exploitative paths, XIT-GFF provides a unified solution to active GDM in unknown cluttered environments that naturally adapts between environmental exploration and critical gas structure exploration whilst exploiting key gas regions en route, without requiring manual clustering or predefined spatial partitions.

Physical validation in a scaled indoor CO₂ release experiment demonstrates real-world feasibility, with XIT successfully navigating and mapping a complex two-source scenario with asymmetric airflow patterns producing overlapping complex plume regions. Although developed for GDM, the framework's structure, combining information-guided sampling, multi-objective tree expansion, and frontier-based goal selection, provides a readily applicable template for robotic information gathering tasks in unknown environments that undoubtedly face the exploration-exploitation trade-off. Future work includes extending the framework to incorporate semantic information in goal evaluation, evaluating performance in larger-scale outdoor scenarios, and investigating the integration of predictive dispersion models to improve gas map convergence during the earlier stages of the active GDM task.

REFERENCES

[1] R. R. Murphy, J. Peschel, C. Arnett, and D. Martin, "Projected needs for robot-assisted chemical, biological, radiological, or nuclear (cbn) incidents," *2012 IEEE International Symposium on Safety, Security, and Rescue Robotics, SSRR 2012*, 2012.

[2] A. Francis, S. Li, C. Griffiths, and J. Sienz, "Gas source localization and mapping with mobile robots: A review," *Journal of Field Robotics*, vol. 39, pp. 1341–1373, 12 2022.

[3] J. G. Monroy, J. L. Blanco, and J. Gonzalez-Jimenez, "Time-variant gas distribution mapping with obstacle information," *Autonomous Robots*, vol. 40, pp. 1–16, 1 2016.

[4] C. Stachniss, C. Plagemann, A. J. Lilienthal, and W. Burgard, "Gas distribution modeling using sparse gaussian process mixture models," in *Robotics : science and systems IV*, vol. 4, 2008, pp. 310–317.

[5] A. J. Lilienthal, M. Reggente, M. Trinca, J. L. Blanco, and J. Gonzalez, "A statistical approach to gas distribution modelling with mobile robots - the kernel dm+v algorithm," *2009 IEEE/RSJ International Conference on Intelligent Robots and Systems, IROS 2009*, pp. 570–576, 12 2009.

[6] T. Wiedemann, C. Manss, and D. Shutin, "Multi-agent exploration of spatial dynamical processes under sparsity constraints," *Autonomous Agents and Multi-Agent Systems*, vol. 32, no. 1, pp. 134–162, 2018.

[7] P. Ojeda, J. Monroy, and J. Gonzalez-Jimenez, "Robotic gas source localization with probabilistic mapping and online dispersion simulation," *IEEE Transactions on Robotics*, vol. 40, pp. 3551–3564, 2024.

[8] C. Rhodes, C. Liu, and W. H. Chen, "Structurally aware 3d gas distribution mapping using belief propagation: A real-time algorithm for robotic deployment," *IEEE Transactions on Automation Science and Engineering*, 2023.

[9] ———, "Scalable probabilistic gas distribution mapping using gaussian belief propagation," *IEEE International Conference on Intelligent Robots and Systems*, vol. 2022-October, pp. 9459–9466, 2022.

[10] S. Bai, T. Shan, F. Chen, L. Liu, and B. Englot, "Information-driven path planning," *Current Robotics Reports*, vol. 2, no. 2, pp. 177–188, 2021.

[11] M. Popović, J. Ott, J. Rückin, and M. J. Kochenderfer, "Learning-based methods for adaptive informative path planning," *Robotics and Autonomous Systems*, vol. 179, p. 104727, 2024.

[12] S. Karaman and E. Frazzoli, "Sampling-based algorithms for optimal motion planning," *The International Journal of Robotics Research*, vol. 30, no. 7, pp. 846–894, 2011.

[13] G. A. Hollinger and G. S. Sukhatme, "Sampling-based robotic information gathering algorithms," *The International Journal of Robotics Research*, vol. 33, no. 9, pp. 1271–1287, 2014.

[14] M. G. Jadidi, J. V. Miro, and G. Dissanayake, "Sampling-based incremental information gathering with applications to robotic exploration and environmental monitoring," *The International Journal of Robotics Research*, vol. 38, no. 6, pp. 658–685, 2019.

[15] L. Schmid, M. Pantic, R. Khanna, L. Ott, R. Siegwart, and J. Nieto, "An efficient sampling-based method for online informative path planning in unknown environments," *IEEE Robotics and Automation Letters*, vol. 5, no. 2, pp. 1500–1507, 2020.

[16] B. Lindqvist, A. Patel, K. Löfgren, and G. Nikolakopoulos, "A tree-based next-best-trajectory method for 3D UAV exploration," *IEEE Transactions on Robotics*, vol. 40, pp. 3496–3513, 2024.

[17] A. Asgharivaskasi and N. Atanasov, "Semantic octree mapping and shannon mutual information computation for robot exploration," *IEEE Transactions on Robotics*, vol. 39, no. 3, pp. 1910–1928, 2023.

[18] J. Rückin, F. Magistri, C. Stachniss, and M. Popović, "An informative path planning framework for active learning in uav-based semantic mapping," *IEEE Transactions on Robotics*, vol. 39, no. 6, pp. 4279–4296, 2023.

[19] J. A. Placed, J. Strader, H. Carrillo, N. Atanasov, V. Indelman, L. Carbone, and J. A. Castellanos, "A survey on active simultaneous localization and mapping: State of the art and new frontiers," *IEEE Transactions on Robotics*, vol. 39, pp. 1686–1705, 6 2023.

[20] J. D. Gammell, S. S. Srinivasa, and T. D. Barfoot, "Batch informed trees (bit*): Sampling-based optimal planning via the heuristically guided search of implicit random geometric graphs," *Proceedings - IEEE International Conference on Robotics and Automation*, vol. 2015-June, pp. 3067–3074, 6 2015.

[21] P. Neumann, V. H. Bennetts, and M. Bartholmai, "P5.4 adaptive gas source localization strategies and gas distribution mapping using a gas-sensitive micro-drone," *Tagungsband*, pp. 800–809, 5 2012.

[22] B. Luo, Q. H. Meng, J. Y. Wang, B. Sun, and Y. Wang, "Three-dimensional gas distribution mapping with a micro-drone," *Chinese Control Conference, CCC*, vol. 2015-September, pp. 6011–6015, 9 2015.

[23] J. Burgués, V. Hernández, A. J. Lilienthal, and S. Marco, "Smelling nano aerial vehicle for gas source localization and mapping," *Sensors*, vol. 19, no. 3, p. 478, 2019.

[24] P. P. Neumann, S. Asadi, A. J. Lilienthal, M. Bartholmai, and J. H. Schiller, "Autonomous gas-sensitive microdrone: Wind vector estimation and gas distribution mapping," *IEEE Robotics and Automation Magazine*, vol. 19, pp. 50–61, 3 2012.

[25] A. Lilienthal and T. Duckett, "Building gas concentration gridmaps with a mobile robot," *Robotics and Autonomous Systems*, vol. 48, no. 1, pp. 3–16, 2004.

[26] M. Reggente and A. J. Lilienthal, "Using local wind information for gas distribution mapping in outdoor environments with a mobile robot," *Proceedings of IEEE Sensors*, pp. 1715–1720, 2009.

[27] C. Rhodes, C. Liu, and W. H. Chen, "Informative path planning for gas distribution mapping in cluttered environments," *IEEE International Conference on Intelligent Robots and Systems*, pp. 6726–6732, 10 2020.

[28] C. Ercolani, L. Tang, A. A. Humne, and A. Martinoli, "Clustering and informative path planning for 3d gas distribution mapping: Algorithms and performance evaluation," *IEEE Robotics and Automation Letters*, vol. 7, pp. 5310–5317, 4 2022.

[29] A. Gongora, J. Monroy, F. Rahbar, C. Ercolani, J. Gonzalez-Jimenez, and A. Martinoli, "Information-driven gas distribution mapping for autonomous mobile robots," *Sensors (Switzerland)*, vol. 23, 6 2023.

[30] R. V. Nanavati, C. Rhodes, M. J. Coombes, and C. Liu, "Low-to-high resolution path planner for robotic gas distribution mapping," in *2024 IEEE International Conference on Robotics and Automation (ICRA)*, 2024, pp. 8457–8463.

[31] A. Gongora, J. Monroy, and J. Gonzalez-Jimenez, "Joint estimation of gas and wind maps for fast-response applications," *Applied Mathematical Modelling*, vol. 87, pp. 655–674, 2020.

[32] M. Wang, B. Xin, M. Jing, and Y. Qu, "An exploration-enhanced search algorithm for robot indoor source searching," *IEEE Transactions on Robotics*, vol. 40, pp. 4160–4178, 2024.

[33] S. Kim, J. Seo, H. Jang, C. Kim, M. Kim, J. Pyo, and H. Oh, "Gas source localization in unknown indoor environments using dual-mode information-theoretic search," *IEEE Robotics and Automation Letters*, vol. 10, no. 1, pp. 588–595, 2025.

[34] Y. A. Prabowo, B. R. Trilaksono, E. M. Hidayat, and B. Yuliarto, "Utilizing a rapidly exploring random tree for hazardous gas exploration in a large unknown area," *IEEE Access*, vol. 10, pp. 15 336–15 347, 2022.

[35] M. Keidar and G. A. Kaminka, "Efficient frontier detection for robot exploration," *International Journal of Robotics Research*, vol. 33, no. 2, pp. 215–236, Feb. 2014.

[36] K. Katyal, K. Popek, C. Paxton, P. Burlina, and G. D. Hager, "Uncertainty-aware occupancy map prediction using generative networks for robot navigation," in *2019 International Conference on Robotics and Automation (ICRA)*, 2019, pp. 5453–5459.

[37] S. M. LaValle, *Planning algorithms*. Cambridge university press, 2006.

[38] J. Monroy, V. Hernandez-Bennetts, H. Fan, A. Lilienthal, and J. Gonzalez-Jimenez, "Gaden: A 3d gas dispersion simulator for mobile robot olfaction in realistic environments," *Sensors 2017, Vol. 17, Page 1479*, vol. 17, p. 1479, 6 2017.

[39] S. Macenski and I. Jambrecic, "SLAM Toolbox: SLAM for the dynamic world," *Journal of Open Source Software*, vol. 6, no. 61, p. 2783, 2021.